Nanoscale

REVIEW

View Article Online
View Journal | View Issue

Cite this: *Nanoscale*, 2024, **16**, 17654

Metal halide perovskite polymer composites for indirect X-ray detection

Shruti Jayaprakash Saiji, [a,b] Yiteng Tang, [a] Shin-Tson Wu, [b] Luis Stand, [c] Yauhen Tratsiak [c] and Yajie Dong *[a,b]

Metal halide perovskites (MHPs) have emerged as a promising class of materials for radiation detection due to their high atomic numbers and thus high radiation absorption, tunable and efficient luminescent properties and simple solution processability. Traditional MHP scintillators, however, suffer from environmental degradation, spurring interest in perovskite–polymer composites. This paper reviews recent developments in these composites tailored for scintillator applications. It discusses various synthesis methods, including solution-based and mechanochemical techniques, that enable the formation of composites with enhanced performance metrics such as light yield, detection limit, and environmental stability. The review also covers the remaining challenges and opportunities in fabrication techniques and performance metric evaluations of this class of materials. By offering a comprehensive overview of current research and future perspectives, this paper underscores the potential of perovskite–polymer composites to revolutionize the field of radiation detection.

Received 2nd July 2024,
Accepted 1st September 2024

DOI: 10.1039/d4nr02716g

rsc.li/nanoscale

1. Introduction

Metal halide perovskites (MHPs) are gaining prominence in photonics and optoelectronics due to their superior photophysical, electrical, and structural properties.[1–3] Notably, their key attributes include high optical absorption, high photoluminescence quantum yields (PLQY), high carrier mobility, and long diffusion lengths. MHPs also exhibit low trap densities and facile solution processability, enhancing their applicability in various energy conversion applications. MHPs have demonstrated potential in light emitting diodes,[4] solar cells[5–7] and photodetectors[8] or radiation detectors, indicating their versatility. Among these, radiation detection stands out as a particularly promising application area for MHPs.[9]

Radiation detectors are crucial across various sectors, including medical imaging,[10] nuclear physics,[11] space exploration,[12] environmental monitoring,[13] and security systems.[14] They detect ionizing radiation energies ranging from low-energy X-rays (keV to hundreds of keV) to gamma rays with emission energies in the giga electron volts (GeV). For X-ray detection, there are two main radiation detection and conversion architectures, direct and indirect. Direct detection relies on the photoconductive material (semiconductors) to absorb and convert ionizing radiation directly into electrical charges. While direct detectors are straightforward in their operation, they are less frequently used in the field because of their relatively high cost and material limitations, such as the need for high-quality semiconductors that can effectively balance stopping power and charge collection efficiency.[15] Nevertheless, silicon (Si), amorphous selenium (a-Se),[16] high purity germanium (HPGe), and cadmium zinc telluride (CZT)[17] are widely used in low X-ray detection systems,[18] X-ray imaging,[19] gamma-ray spectroscopy[20,21] and the newly developed CZT-based single-photon emission computed tomography (SPECT).[22] Perovskites have been considered for direct conversion due to their promising properties, but achieving an optimal balance between X-ray absorption and charge collection remains a significant challenge. To effectively capture high-energy X-rays, a thicker detector is necessary to ensure sufficient interaction with the penetrating X-rays. However, this increase in thickness involves a trade-off, as it complicates the design and can lead to higher charge loss and recombination, ultimately reducing overall efficiency. The development of perovskite-based direct detectors is beyond the scope of this review; interested readers can refer to other specialized publications for more detailed information on this topic.[23,24] In contrast, indirect detection uses a scintillator, a material that converts high-energy radiation into optical photons. These

[a]*NanoScience Technology Center, Department of Materials Science and Engineering, University of Central Florida, Orlando, Florida, 32826, USA.*
E-mail: yajie.dong@ucf.edu
[b]*College of Optics and Photonics, University of Central Florida, Orlando, Florida, 32826, USA*
[c]*Scintillation Materials Research Center, University of Tennessee, Knoxville, Tennessee, USA*

photons are then collected by photodetector, such as a photomultiplier tube (PMT) or silicon photomultiplier (SiPM), which converts them into an electrical signal. Indirect conversion is the dominant radiation detection method for many national security and medical imaging applications due to the excellent cost-to-performance ratio offered by scintillator-based detectors.

Traditionally, solid scintillators are classified into two main categories: inorganic and organic/plastic scintillators. Inorganic scintillators are known for their high density and atomic number, which enhance their efficiency in stopping and detecting X-rays, along with a high light yield that results in better signal strength and resolution. Additionally, they offer good energy resolution and stability, ensuring consistent performance over time. Inorganic scintillators like thallium-doped sodium iodide (NaI:Tl) and cesium iodide (CsI:Tl), europium-doped lithium iodide (LiI:Eu), cerium doped lanthanum bromide ($LaBr_3$:Ce), terbium-doped gadolinium oxysulfide (Gd_2O_2S:Tb),[25] cadmium tungstate ($CdWO_4$) and cerium doped lutetium orthosilicate (Lu_2SiO_5:Ce),[26] are widely used in border-crossing portal monitors,[27] hand-held and mobile radiation detection systems, high and low X-ray imaging devices. However, they can be more expensive and challenging to manufacture, with some materials being brittle and susceptible to damage.[28] On the other hand, organic and particularly plastic scintillators are flexible, easy to fabricate into various shapes and sizes, and generally more rugged and less prone to damage. Despite these advantages, they have lower density and atomic number, leading to reduced efficiency in X-ray detection, and they produce less light per unit of absorbed radiation, impacting signal strength and energy resolution. Consequently, they typically offer poorer energy resolution compared to inorganic scintillators.[29,30]

Composite scintillators, which combine inorganic and organic scintillators, aim to leverage the benefits of both types: the high density and atomic number of inorganic materials for efficient X-ray absorption, and the fast response times and flexibility of organic materials. These composites can potentially offer improved light yield, faster decay times, and better energy resolution, making them suitable for diverse applications like medical imaging and security screening.[31,32] However, creating effective composites from traditional scintillators presents challenges. Inorganic and organic materials often have different thermal and mechanical properties, complicating the fabrication process and stability. Ensuring uniform mixing and consistent performance across the composite is difficult due to variations in scintillation properties. Additionally, optimizing the interface between the components to ensure efficient energy transfer and minimize quenching effects is crucial.

Metal halide perovskites (MHPs) are emerging as promising scintillator materials due to their exceptional photonic properties.[33–35] MHPs have been initially studied in single-crystal and nanoparticle forms, demonstrating high light yield, excellent energy resolution, and tunable emission wavelengths, which make them highly attractive for X-ray detection applications.[36] Their high atomic numbers contribute to efficient X-ray absorption, while their defect tolerance allows for high luminescence efficiency even in the presence of material imperfections.

Despite these promising merits, MHPs in single-crystal and nanoparticle forms face significant limitations. Single crystals, while offering superior scintillation performance, are challenging to grow, and their brittleness limits their practical applications, especially in large-scale detectors.[37] Nanoparticles, on the other hand, suffer from issues related to aggregation, stability, and the need for surface passivation to maintain their scintillation properties. Additionally, both forms may have issues with scalability and integration into existing detection systems.[38,39]

To address these limitations, perovskite–polymer composites are being explored as a potential solution. MHPs are uniquely suitable for composite scintillators due to their easy solution processability and high light yield in nanoparticle forms. In composite form, MHPs can be embedded within a polymer matrix, combining the high scintillation efficiency of perovskites with the mechanical flexibility and processability of polymers. These composites can be easily fabricated into various shapes and sizes, making them suitable for a wide range of applications. The polymer matrix can also provide protection to the perovskite particles, enhancing their stability and durability.[40] Moreover, perovskite–polymer composites can potentially overcome the scalability issues associated with single crystals and nanoparticles. They offer the possibility of large-area, flexible scintillators that can be produced through cost-effective manufacturing techniques such as solution processing or extrusion. This makes them an attractive option for developing next-generation indirect X-ray detectors that are both high-performing and practical for widespread use.

This review provides a comprehensive overview of recent advancements in metal halide perovskite polymer composites for indirect X-ray detection. We begin with a general introduction to MHPs, highlighting their crystal structure and various forms, ranging from three-dimensional to lower-dimensional structures. We then explore the scintillation process, discussing the underlying mechanisms and performance metrics. Next, we cover the synthesis techniques for perovskite scintillator components and their incorporation into perovskite–polymer composites. The review further perovskite–polymer composites for indirect X-ray detection, with a focus on 3D lead-based, 2D lead-based, and lead-free composites. Finally, we discuss the performance, stability, and environmental resilience of these composites, concluding with perspectives on current challenges and future research directions in MHP polymer composite scintillators.

2. General introduction to metal halide perovskites

2.1 Crystal structure of perovskites

Perovskites are materials defined by a distinctive crystal structure with the general formula ABX_3. In this structure, A rep-

resents an organic cation such as methylammonium ($CH_3NH_3^+$), formamidinium ($CH(NH_2)_2^+$), or an inorganic cation like cesium (Cs^+); B is a smaller metal cation such as lead (Pb^{2+}), tin (Sn^{2+}), copper (Cu^{2+}), or manganese (Mn^{2+}); and X is a halide anion like iodide (I^-), bromide (Br^-), or chloride (Cl^-) (shown in Fig. 1a).[41] Depending on the dimensions and connectivity of their constituent octahedra (BX_6 units), perovskites can be categorized as three-dimensional (3D), two-dimensional (2D), one-dimensional (1D), or zero-dimensional (0D). In addition, they can also be classified based on their physical form, such as nanosheets, nanorods/wires, and quantum dots. 3D metal halide perovskites have shown promising scintillation properties.[33] However, these materials in the single crystal form, perform well only at low temperatures because high temperatures can induce thermal quenching effects that degrade their scintillation properties and efficiency.[42,43] In lower dimensional perovskites, 2D perovskites have the formula A_2BX_4, where A is an organic cation, B is a metal cation such as lead (Pb) or tin (Sn), X is a halide anion. Examples include butylammonium lead bromide (BA_2PbBr_4) and phenylethyl ammonium lead iodide (PEA_2PbI_4). 2D perovskites have a layered structure with perovskite sheets separated by organic spacers[41] as shown in Fig. 1b. This structure imparts 2D perovskites with enhanced stability against moisture, oxygen, and light, as well as strong quantum confinement effects leading to higher exciton binding energies.[44] Transitioning from 2D to lower dimensional perovskites, the incorporation of larger or bulkier cations can introduce steric hindrance or strain, disrupting the continuous two-dimensional connectivity and leading to the formation of discrete clusters or isolated regions within the larger 2D structure, ultimately resulting in 1D and 0D structures[45–47] (Fig. 1d and e). A distinct category within perovskite materials is that of double perovskites, featuring variations where the B site in the conventional ABX_3 perovskite structure can host two distinct cations, leading to a $A_2B'B''X_6$ structure with double B-site occupation, with X representing halide ions[41,48] (Fig. 1c).

Besides changing perovskite dimension or the chemical composition, doping is an efficient method to tailor the perovskite properties. Mn^{2+} doping in 3D lead perovskites, for instance, involves substituting the Pb^{2+} cations in the octahedral structures, and has been reported to enhance properties like luminescence and stability[49,50] (Fig. 1f). Alongside lead-based perovskites, lead free perovskites are emerging as an attractive and fast developing area due to their non-toxicity and environmental friendliness. Metal halide perovskites with cations such as tin, germanium, bismuth, antimony, copper, manganese have been reported as alternatives to lead based perovskites.[51] Several lead-free metal halides, particularly those based on copper and manganese, have been reported for scintillation applications.[52–54]

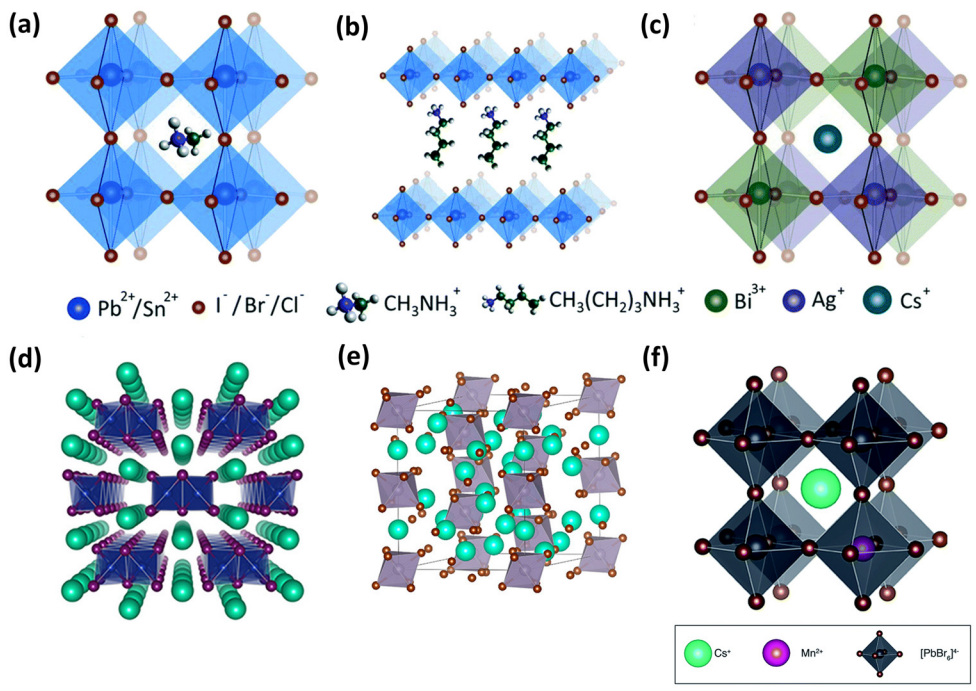

Fig. 1 Schematic crystal structure of perovskites. (a) 3D perovskites (b) 2D perovskites with a layered structure and (c) lead free double perovskites. Reproduced with permission from ref. 41. Copyright 2016 Royal Society of Chemistry. (d) 1D perovskite structure of $CsCu_2I_3$. Reproduced with permission from ref. 45. Copyright 2021 American Chemical Society. (e) 0D perovskite structure of Cs_4SnBr_6. Reproduced with permission from ref. 47. Copyright 2020 American Chemical Society. (f) Mn^{2+} doped 3D lead perovskites. Reproduced with permission from ref. 49. Copyright 2013 Royal Society of Chemistry.

3. Scintillation process

3.1 Mechanism

The scintillation mechanisms in organic and inorganic materials are different due to their distinct chemical compositions and structural properties. Organic scintillators consist of aromatic compounds or polymers with complex molecular structures. Scintillation in these materials occurs when high-energy radiation interacts directly with the organic molecules, exciting electrons to higher energy levels within their molecular orbitals. Upon relaxation back to their ground state, these excited electrons emit photons, resulting in scintillation. In inorganic materials, scintillation is a complex multistep process where high-energy photons or charge particles undergo interactions with the scintillator material, through the well-known mechanisms of radiation interactions in matter, briefly described below, leading to the creation of excited states within the scintillator material's crystalline structure. As these excited states relax to lower energy levels, they emit photons, resulting in scintillation. Due to the more complex and efficient energy transfer and relaxation processes within the crystalline lattices, inorganic scintillators generally exhibit higher light yields but with a slower decay time than organic scintillators.[55]

In inorganic scintillators, the three main types of radiation interaction with the material are photoelectric effect, Compton scattering, and pair production. The photoelectric effect, where photons are absorbed by atoms within the material, ejecting electrons from inner shells is the dominant process when using X-rays or low-energy γ-rays (less than a few hundred keV).[56,57] Here, the absorption coefficient (μ) is proportional to:

$$\mu \propto \frac{\rho Z^n}{E^{3.5}}, \tag{1}$$

where n ranges from 3 to 4, Z is the atomic number, ρ is the scintillator density, and E is the photon energy. The presence of heavy atoms in the scintillation material significantly enhances the absorption of X-rays and low-energy γ-rays. For X-ray and γ-ray energies ranging from a few hundred keV to approximately 1 MeV, Compton scattering becomes the dominant interaction. In Compton scattering, photons collide with free or loosely bound electrons, transferring energy to the electrons and excites them to a higher energy level.[58,59] In this process, the absorption coefficient (μ) is proportional to:

$$\mu \propto \frac{\rho}{E^{0.5}}. \tag{2}$$

The effectiveness of the scintillator in this range depends primarily on the material's density, with the main process being the generation of low-energy electron–hole pairs. At energies above 1 MeV, pair production becomes the primary interaction. The absorption coefficient (μ) can be expressed as:

$$\mu \propto \rho Z \ln\left(\frac{2E}{m_e c^2}\right), \tag{3}$$

where m_e is the electron mass and c is the speed of light. This process results in the formation of electron–positron pairs, with the positrons eventually annihilating with electrons.[60] Therefore, the effectiveness of scintillators across different energy ranges depends on factors such as the presence of heavy atoms for low-energy interactions and the material's density for higher-energy interactions.

Soon after ionization of the scintillator material, primary electron–hole (e–h) pairs are created, initiating a cascade of secondary excitations produced through inelastic scattering and Auger processes, where energy is transferred non-radiatively between electrons. At around 10^{-16} to 10^{-14} seconds, exciton multiplication ceases, leading to the thermalization of electronic states, where excess energy is dissipated through interactions with the lattice vibrations (phonons) of the material. At this stage, thermalized electrons migrate to the bottom of the conduction band and holes move to the top of the valence band. Next, around 10^{-12} and 10^{-10} seconds, some free electrons and holes localize at stable defects or material impurities, leading to formation of self-trapped excitons (STE) and self-trapped holes (STH). From 10^{-10} to 10^{-8} seconds, e–h pairs transfer their energy to the luminescence centres leading to their excitation. Finally, the excited luminescence centre, radiatively relaxes to its ground state producing scintillation light.[61,62]

3.2 Performance metrics

3.2.1. Light yield. Light yield (LY) or light output quantifies a scintillator's efficiency in converting ionizing radiation into visible light. It is defined as the number of photons emitted per unit of energy deposited (measured in MeV) and is expressed in photons per MeV (photons per MeV). The light yield can be theoretically calculated[28] using the following equation:

$$L = \frac{n_{e-h}}{E_i} SQ = \frac{\left(\frac{E_i}{\beta E_g}\right)}{E_i} SQ = \frac{SQ}{\beta E_g}, \tag{4}$$

where n_{e-h} is the number of electron–hole pairs created by the incident ionizing radiation, E_i is the incident radiation energy, E_g is the bandgap energy of the scintillator material, β is a constant parameter that represents the average energy required to generate one electron–hole pair, S and Q are the quantum efficiencies of the carrier transport and recombination processes, respectively.

In practice, determining the absolute light yield (LY) involves using a photodetector such as a photomultiplier tube (PMT). For this, the following parameters are essential: (i) the PMT's quantum efficiency (QE_{PMT}), provided by the manufacturer, which indicates the number of electrons created per incident photon of a given wavelength (%), and (ii) the total number of photoelectrons (LY_{phe}) emitted by the photocathode in a scintillation event of known gamma-ray energy, typically Cesium-137 (Cs-137).[63] The LY_{ph} in photons per MeV is then given by:

$$LY_{ph} = \frac{LY_{phe}}{R_s T_s(x^*) QE_{PMT}}, \tag{5}$$

where the $R_sT_s(x^*)$ term accounts for the reflections and self-absorption of the scintillation photons before they reach the detector. When using a silicon avalanche photodiode (APD) as the photodetector, the quantum efficiency QE_{PMT} is replaced by QE_{APD}, reflecting how APDs convert incident photons into electron–hole pairs rather than directly into photoelectrons and LY_{phe} is replaced by LY_{eh}, which is the total number of electron–hole pairs created in a scintillation event of know gamma-ray energy.

In scintillator characterization, two commonly used methods for assessing LY are the pulse height spectra analysis and the comparison method. Pulse height spectra analysis involves examining the distribution of electrical pulse heights generated by scintillation events in response to ionizing radiation.[64,65] Sources like Americium-241 (Am-241) and Cesium-137 (Cs-137) are frequently used in pulse height spectra measurements to benchmark scintillator performance against established standards. In the comparison method for measuring LY in scintillator materials, the LY is quantified by comparing the integrated areas under the radioluminescence (RL) spectra of both the unknown scintillator and a reference material with known characteristics. In the comparison method, integrating spheres are used to measure the RL spectra, providing a controlled environment that enhances the accuracy and reproducibility of LY measurements. The scintillator sample can be positioned inside the integrating sphere for uniform light collection and controlled measurement conditions, or outside the sphere to offer greater flexibility in sample handling. However, regardless of the setup, it is crucial to ensure that both samples have similar attenuation coefficients. This approach minimizes the influence of attenuation differences on the LY measurement, allowing for a more reliable characterization of the scintillator materials.

3.2.2. Mass attenuation coefficient. The mass attenuation coefficient ($cm^2\ g^{-1}$) is a crucial parameter in radiation physics that measures how effectively a material attenuates radiation per unit mass. It provides a normalized measure that facilitates comparisons between materials of different densities. In metal halide perovskites containing elements with high atomic masses, such as lead, the mass attenuation coefficient is enhanced by increasing the likelihood of radiation interactions. However, in polymer–perovskite composites, the mass attenuation coefficient value also depends significantly on the density of the composite material. Thus, improving perovskite loading becomes crucial as polymers typically have lower density structures, impacting overall attenuation efficiency.[34]

3.2.3. Spatial resolution. Spatial resolution refers to the detector's ability to distinguish two neighboring objects with high reproduction fidelity. This is crucial in medical imaging applications where early disease detection is paramount to reducing cancer-related deaths and improving patient outcomes. Spatial resolution is quantified using the Modulation Transfer Function (MTF). It expresses the fidelity by which the object information is transferred to the image as a function of spatial frequency in the object. Spatial frequency, measured in "line pairs per millimeter", directly relates to spatial resolution by indicating how many distinct line pairs can be resolved within one millimetre. Thus, spatial resolution is often expressed in terms of lp mm^{-1} to quantify the detector's ability to reproduce high-resolution images accurately, though it can also be described in length units such as micrometers (μm) or millimeters (mm), which reflect the smallest distance between distinguishable features.

3.2.4. Detection limit. The detection limit of a scintillator indicates the minimum level of ionizing radiation it can reliably detect and convert into measurable signals. This limit is measured in units of radiation dose rate, such as $nGy_{air}s^{-1}$ (nanograys per second in air) or $\mu Gy_{air}s^{-1}$ (micrograys per second in air), where one gray (Gy) is the absorption of one Joule of radiation energy per kilogram of matter. In conventional X-ray diagnosis, a detection limit of 5.5 $\mu Gy_{air}s^{-1}$ is required.[66] Metal halide perovskite based X-ray scintillator detectors with a much lower detection limit of 13 $nGys^{-1}$ have been reported[33] although concerns may remain regarding the standardization of the detection limit determination.[67]

3.2.5. Radiation hardness. Radiation hardness refers to a scintillator's ability to maintain functionality under prolonged radiation exposure. This is tested by measuring radioluminescence (RL), the visible or near-visible light emitted by a scintillator when excited by ionizing radiation, before, during, and after controlled radiation exposure. This verifies whether consistent light output and signal stability are maintained despite the absorbed dose of ionizing radiation. This property is crucial for applications like medical imaging (PET scans), security screening (airport scanners), and high-energy physics experiments (particle detectors), where the scintillator material will be exposed to ionizing radiation for long durations.

3.2.6 Moisture and thermal stability. Environmental factors such as temperature, humidity, and exposure to atmospheric gases can significantly impact the stability of scintillators, affecting their light emission efficiency. High temperature and humidity can cause water penetration into the scintillator material, leading to fogging, reduced transparency, increased light scatter, and degraded detection performance. Plastic scintillators like PVT are susceptible to fogging with daily temperature and humidity cycles, which deteriorate their effectiveness over time.[68–70] The use of metal halide perovskites in scintillator applications is also significantly challenged by their moisture susceptibility. However, polymer-perovskite composites show promise in this regard, with reports of improved stability.[40]

3.2.7 Decay time. The decay time of a scintillator refers to the duration it takes for the intensity of the emitted light pulse to decrease to $1/e$ (~37%) of its maximum value after excitation. Traditional inorganic scintillators like Bismuth Germanate (BGO) and Lutetium Yttrium Orthosilicate (LYSO) typically have decay times of 300–700 ns and 30–40 ns, respectively.[65] Lead-based metal halide perovskite scintillators like $CsPbBr_3$ have a reported decay time of 8.09 ns.[71] In contrast, lead-free metal halides, such as those containing manganese and copper, typically show much longer decay times in the

microsecond range. For instance, $Cs_3Cu_2I_5$ has been reported with a decay time in microseconds.[72]

3.2.8 Emission colour. The emission colour of a scintillator is crucial because it determines the compatibility with various photodetectors. Different photodetectors are optimized to detect specific wavelengths of light, enhancing overall system efficiency and sensitivity. Common photodetectors used in scintillator light detection include photomultiplier tubes (PMTs), silicon photomultipliers (SiPMs), photodiodes, and charge-coupled devices (CCDs). PMTs are highly sensitive to blue and ultraviolet light, typically covering a spectral range from around 300 to 650 nm, with peak sensitivity near 400 nm. SiPMs, in contrast, are sensitive across a broader range, from 300 to 900 nm, with peak sensitivity in the visible spectrum. Photodiodes and CCDs also provide high efficiency across the visible light spectrum, ensuring excellent spatial resolution and signal detection.[73] MHPs are uniquely suited for scintillator applications due to their ability to emit light in various colours. This tunability is achieved by altering their chemical composition, which allows for precise matching with different photodetectors.[74,75] Efficient green emission from perovskites, for instance, matches well with the peak sensitivity of low-cost, high-performance, highly compact, Si-based photodetectors. This capability is a significant advantage, as it allows for the design of scintillators tailored to specific detection needs, enhancing performance and broadening potential applications.

4. Synthesis methods

4.1 Metal halide perovskite components

In this section, we will briefly discuss the commonly used synthesis methods for metal halide perovskite components used in polymer composites for scintillator applications. We divide the methods broadly into two categories: solution-based chemical synthesis techniques and mechanochemical methods. Solution-based chemical synthesis techniques encompass methods that initiate nanomaterial formation from molecular or ionic precursors, typically within a solvent environment. In this category, we will focus on some commonly used methods such as hot injection and precipitation methods like the ligand-assisted reprecipitation (LARP) method. Additionally, we will discuss synthesis methods used for growing lead-free single crystal metal halides, such as the hydrothermal method. Finally, mechanochemical methods like ball milling will be covered, where mechanical energy is utilized to induce chemical reactions in solid-state materials, often eliminating the need for solvents.

4.1.1 Solution-based chemical synthesis techniques

4.1.1.1. Hot-injection. The hot injection (HI) method, developed over three decades ago, stands as a widely used technique for synthesizing colloidal nanocrystals (NCs).[76] This method involves rapidly injecting a precursor solution into a hot reaction solvent, leading to the nucleation and growth of nanocrystals. Control over the size and shape of nanocrystals is achieved by adjusting ligands, reaction temperature, and precursor ratios. Surface passivation with organic ligands is crucial for stabilizing the nanocrystals and controlling their optical properties. Its extension to perovskite NCs (PNCs),[74] has enabled the synthesis of monodisperse NCs with tunable sizes and compositions[77] (Fig. 2a). Perovskite NCs synthesized using hot injection method have been reported for use in perovskite–polymer composites/films for scintillator applications by several groups.[78] Chen *et al.* synthesized $CsPbX_3$ (X = Cl, Br, I) MHP-NCs through a hot-injection method.[79] Cesium oleate and $PbBr_2$ were used as precursors while oleic acid, oleylamine were used as ligands, with octadecene as the solvent. Varying compositions of $CsPbX_3$ (where X = Cl, Br, I) were obtained by adjusting the molar ratios of Cl/Br or Br/I while keeping the Cs/Pb ratio constant. A variation of this hot injection method was reported by Wang *et al.*[80] The synthesis method for $CsPbBr_3$ NCs involved utilizing Cs_2CO_3 as the source of cesium ions and 2-hexyldecanoic acid as a stabilizing ligand to prevent aggregation of the NCs, instead of the conventional oleic acid. A modified procedure to synthesize $CsPbBr_3$ nanosheets was reported by Wang *et al.*[81] This method differs from the typical hot injection method since the precursors were prepared in air, unlike the conventional practice of using inert conditions, and at a moderately high temperature of 90 °C, using solvents such as 1-propanol and hexane. In addition to nanosheets, dual-phase $CsPbBr_3$@$CsPb_2Br_5$ PNCs were also synthesized using a one-pot hot-injection method by Naresh *et al.*[82] Cerium doped $CsPbBr_3$ perovskite NCs[83] and lead free potassium doped copper halides, like K^+:$Cs_3Cu_2Cl_5$ nanosheets,[84] have been synthesized for scintillator applications. The hot injection method enables precise control over reaction conditions and high-quality nanocrystal production, however, its requirements for specialized equipment like a Schlenk line and high temperature reaction conditions pose scalability challenges for large-scale production needed in radiation detection applications.

4.1.1.2 Hydrothermal method. The hydrothermal method is a widely utilized synthesis technique in chemistry,[85,86] and has been utilized in synthesizing lead free double perovskite single crystals.[42,87] In the hydrothermal method, the precursor solution is heated in a sealed vessel (autoclave) at temperatures typically near the boiling point of the solvent, ranging from 100 °C to 250 °C. The high temperature and pressure promote the dissolution of precursors and facilitate the nucleation and crystal growth. Ligands can also be incorporated into the precursor solution to regulate the growth process and to reduce surface defects. Wang *et al.* utilized the hydrothermal method for the synthesis of cerium doped, lead free double perovskite single crystals of Ce:$Cs_2NaTbCl_6$.[88]

Initially, metal halides CsCl, NaCl, and $ReCl_3{\cdot}6H_2O$ (where Re = Ce, Tb) were dissolved in hydrochloric acid. Subsequently, the resulting mixture was heated at 180 °C in an autoclave for 24 hours. Finally, the autoclave was allowed to cool to room temperature, and the produced crystals were filtered and washed with ethanol. A similar procedure was used by Zhang *et al.* to synthesize single crystals of $Cs_2NaLuCl_6$.[91] A precursor

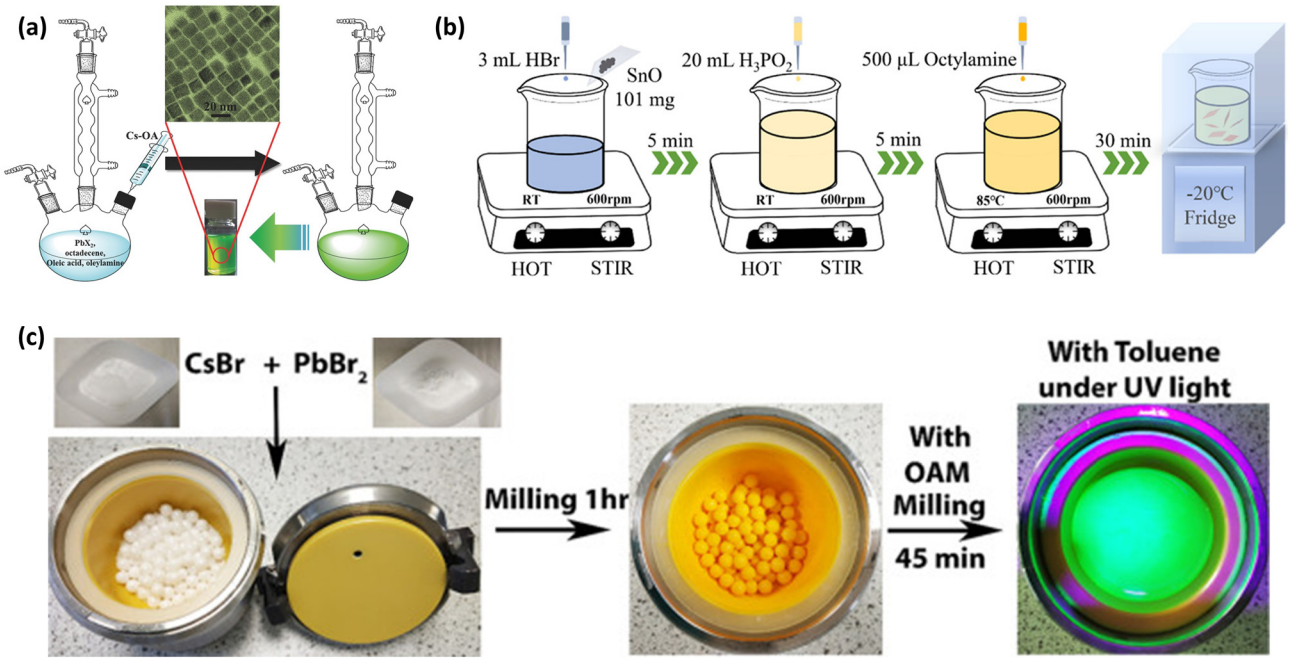

Fig. 2 Synthesis methods of the metal halide perovskites. (a) A schematic showing the hot-injection method. Reproduced with permission from ref. 77. Copyright 2017 John Wiley and Sons. (b) A schematic illustrating the synthesis steps for creating lead free 2D layered $(C_8H_{17}NH_3)_2SnBr_4$ perovskites. Reproduced with permission from ref. 89. Copyright 2020 American Chemical Society. (c) Synthesis steps for $CsPbBr_3$ using the ball milling method. Reproduced with permission from ref. 90. Copyright 2023 American Chemical Society.

mixture of CsCl, NaCl, and Lu_2O_3 in hydrochloric acid was heated in an autoclave to 180 °C, then cooled to room temperature for crystallization. $DyCl_3{\cdot}6H_2O$ and AgCl were added as dopants to obtain the doped $Cs_2Na_{0.9}Ag_{0.1}LuCl_6{:}Dy^{3+}$ double perovskites. The resulting crystals were washed with ethanol and dried at 60 °C. Additionally, the hydrothermal synthesis of $Cs_2CdBr_2Cl_2$, a 2D perovskite, was also reported.[92] Through the incorporation of Mn^{2+} dopants into the perovskite structure, a yellow emission centred at 593 nm with a PLQY of 98.52% was obtained.

4.1.1.3. Precipitation methods. Precipitation methods are a widely utilized technique for synthesizing nanoparticles from the precursor solution.[93] In this approach, two or more precursor compounds are dissolved in a suitable solvent, followed by the addition of a precipitating agent. As the precipitating agent is introduced, the solubility of one or more components in the solution decreases, prompting the formation of solid particles that separate from the solvent. These particles can then be collected through filtration or centrifugation and further processed as necessary. While the hot injection method provides better control over nucleation and growth rates but requires special equipment and an inert atmosphere, the precipitation method offers a simpler alternative, making it more accessible and cost-effective. Moreover, precipitation methods can be readily scaled up to produce nanocrystals in large quantities, making them suitable for commercial production and offering a promising avenue for mass production of NCs for scintillator applications.

In the synthesis of perovskite NCs, various precipitation methods such as the antisolvent method, Ligand-Assisted Reprecipitation Method (LARP),[75,94] and acid precipitation methods are employed to finely tune their size, morphology, and properties. The antisolvent method involves the controlled addition of a nonsolvent to induce precipitation,[95] while LARP utilizes ligands to form complexes with the solute before inducing precipitation with an antisolvent,[96] thereby providing additional control over the resulting nanocrystal properties. In the acid precipitation method, a compound is precipitated from solution by adjusting the pH to acidic conditions.[97] This pH alteration can lead to the formation of insoluble salts or complexes, which then precipitate out of the solution. Several researchers have reported the use of precipitation methods as a more scalable and cost-effective approach to synthesize perovskite NCs for scintillator applications.[98]

Utilizing the antisolvent precipitation method Cao *et al.*,[99] synthesized perovskite NCs with the "emitter in matrix" design $CsPbBr_3@Cs_4PbBr_6$. The CsBr and $PbBr_2$ precursors were dissolved in dimethyl sulfoxide (DMSO) and subjected to rapid toluene addition as an antisolvent. The resulting nanocrystals showcased potential as scintillators for X-ray sensing and imaging. The synthesize of lead-free $Cs_3Cu_2I_5$ polycrystalline powders was reported by Zhou *et al.* using an antisolvent method.[100] CsI and CuI were dissolved in DMSO to form a precursor solution, which was then slowly added to cold 2-propanol under sonication. Immediate white precipitates formed, which were separated by centrifugation and washed with 2-pro-

panol before drying at 70 °C under vacuum overnight. A similar method to obtain $Cs_3Cu_2I_5$ microcrystals using chloroform as the antisolvent was reported.[101] Even with the use of lead-free precursors, the scalability of composite scintillator screens may face challenges if toxic solvents are utilized in the process. Wang *et al.* addressed this issue in their study, by proposing a green synthesis antisolvent method to fabricate lead free $Cs_3Cu_2I_5$ perovskite NCs.[102] Using anhydrous ethanol as the green antisolvent, a high PLQY of 87.2% was achieved for the $Cs_3Cu_2I_5$ NCs. The synthesis of manganese-based metal halides $(TEA)_2MnCl_4$ (TEA = tetraethylammonium) and $(TBA)_2MnCl_4$ (TBA = tetrabutylammonium) single crystals using ethyl ether as the antisolvent was reported.[103] In addition to Cu and Mn, copper doped silver-based metal halide Cs_2AgI_3 polycrystalline powders have also been synthesized using the antisolvent method.[104] CsI and AgI powders (2 : 1 molar ratio) were dissolved in anhydrous DMSO, CuI was added for doping, and the mixture was then added to cold dichloromethane (DCM) under ultrasonication to obtain polycrystalline Cs_2AgI_3.

The method of acid precipitation for perovskite NCs has also been reported for scintillator applications. Zheng *et al.* reported the synthesis of 2D lead-based perovskite $(C_{12}H_{25}NH_3)_2PbBr_4$ (DA_2PbBr_4), using this method.[105] The synthesis involved dissolving dodecylamine ($C_{12}H_{25}NH_2$) in hydrobromic acid and glacial acetic acid by heating. Later, HBr solution of $PbBr_2$ was added to this mixture at 120 °C, the mixture reacts to produce a milky solution. The 2D perovskite was obtained by subsequent rapid cooling and centrifugation. The synthesis of 2D butylammonium lead bromide perovskite, namely BA_2PbBr_4:Mn(II) was also reported.[106] Lead free perovskites like Cs_2ZrCl_6 have also been synthesized using this method.[107] CsCl and $ZrCl_4$ powders, with a molar ratio of 2 : 1, were separately dissolved in HCl. The CsCl solution was slowly mixed into $ZrCl_4$ solution under vigorous stirring, forming a white precipitate. The precipitate was then centrifuged, washed with methanol, and dried at 80 °C for 30 minutes to obtain Cs_2ZrCl_6.

Several groups have also utilized the LARP method to synthesize perovskite NCs for scintillator applications. Gandini *et al.* reported the synthesis of $CsPbBr_3$ using this method, with an emission peak at 518 nm, full width at half maximum of 25 nm and a PLQY of 75 ± 8%.[108] The synthesis of $CsPbBr_3$ for scintillator applications using this method was also reported by Skrypnyk *et al.*[109] In this work, cesium bromide and lead bromide precursors were initially dissolved in *N*,*N*-dimethylformamide (DMF). Then, the ligands *n*-octylamine and oleic acid were added to obtain a transparent, colourless precursor mixture. This mixture was subsequently added to toluene, serving as an antisolvent, with vigorous stirring at room temperature. This process resulted in a bright yellow-green colloidal solution of $CsPbBr_3$ NCs. In addition to inorganic perovskites, organic–inorganic hybrid perovskites like formamidinium lead bromide ($FAPbBr_3$) NCs were also synthesized using this method.[110] The $FAPbBr_3$ NCs were synthesized dissolving lead bromide and formamidinium bromide in DMF to form a precursor solution. Separately, octylamine and oleic acid, serving as ligands, were vigorously mixed in toluene. The addition of the precursor solution to the toluene mixture, acting as an antisolvent, induced immediate nanocrystal precipitation. The resulting nanocrystal dispersion was centrifuged and purified to obtain the $FAPbBr_3$ NCs. The LARP method has also been used to synthesize lead free copper-based metal halides. Han *et al.* employed a modified LARP method to synthesize Rb_2CuX_3 (X = Br, Cl) copper halides for scintillator films.[111] A solution of RbBr, CuBr, and hypophosphorous acid in DMSO was quickly injected into an antisolvent mixture of toluene and oleic acid. After centrifugation and drying, the Rb_2CuBr_3 metal halide was formed, demonstrating a PLQY of 59.06%, with emission peak at 385 nm and a 90 nm Stokes shift.

In addition to the LARP method, a modified precipitation method for the synthesis of hybrid copper-based metal halides was reported. A liquid phase cooling precipitation method was used for the synthesis of $TEA_2Cu_2Br_4$ (TEA = tetraethylammonium).[112] Initially, 2 mmol CuBr and 4 mmol TEABr were dissolved in 10 mL of anhydrous ethanol in a sealed nitrogen environment to prevent Cu^+ oxidation. The solution was heated at 85 °C until complete dissolution. Upon cooling to 25 °C, the solution became supersaturated, resulting in $TEA_2Cu_2Br_4$ formation, with a PLQY of 55%, with emission at 462 nm and a 142 nm Stokes shift.

4.1.1.4. Other solvochemical methods. In addition to the methods described above, other solvochemical methods have also been reported. An acid based method was reported for two dimensional tin based lead-free perovskites.[89] $(C_8H_{17}NH_3)_2SnBr_4$ perovskites were prepared by dissolving stannous oxide (SnO) powder in hydrobromic(HBr) acid, followed by the addition of hypophosphorous acid (H_3PO_2) and dropwise addition of *n*-octylamine to the tin precursor solution (Fig. 2b). The mixture was heated and then slowly cooled to obtain perovskites NCs with a PLQY of 98% with emission at 596 nm and a large Stokes shift of 246 nm. The synthesis of manganese-based metal halides was also reported. The $(C_{38}H_{34}P_2)MnBr_4$ single crystals were obtained using a room temperature solvent diffusion method.[113] In this method, to a dichloromethane (DCM) solution containing triphenylphosphonium bromide ($C_{38}H_{34}P_2Br_2$) and $MnBr_2$ in equal proportions, diethyl ether was introduced to facilitate their reaction.

One of the common solvochemical methods used for the synthesis of metal halide crystals is slow solvent evaporation induced crystallization. In this method, a solution containing the desired solute is allowed to evaporate gradually under controlled conditions, leading to the formation of single crystals. By evaporating the solvent slowly, the concentration of the solute increases over time, eventually reaching a point where the solute precipitate out of solution and form crystals. This method is commonly used to grow high-quality single crystals with well-defined structures, particularly when the solute has limited solubility in the chosen solvent. The synthesis of zero-dimensional $(BTPP)_2MnX_4$ (BTPP = benzyltriphenylphospho-

nium; X = Cl, Br) was reported using a slow solvent evaporation method.[114] BTPPBr (2 mmol) and $MnBr_2$ (1 mmol) were dissolved in a mixed solvent of HBr solution (4 mL) and ethanol (7 mL) and then slowly evaporated at 50 °C for 2–3 days. The resulting product was washed with ethanol to obtain single crystals of $(BTPP)_2MnBr_4$. Copper based metal halides were also synthesized using this method. (TBA)CuX_2, where TBA represents tetrabutylammonium cation and X stands for either Cl or Br, were synthesized *via* a slow solvent evaporation method at room temperature.[115] The (TBA)$CuCl_2$ and (TBA)$CuBr_2$ single crystals exhibited green and blue emissions, peaking at 510 nm and 498 nm, respectively. They displayed large Stokes shifts of 224 nm and 209 nm and achieved high PLQYs of 92.8% and 80.5% for (TBA)$CuCl_2$ and (TBA)$CuBr_2$ single crystals (SCs), respectively.

4.1.2 Mechanochemical methods

4.1.2.1. Ball milling. To fabricate cost-effective perovskite–polymer composite scintillators, it is essential to develop scalable methods for the synthesis of perovskite NCs. Current methods, such as hot injection, LARP, and anti-solvent techniques involve high temperatures and toxic solvents. Overcoming these challenges is crucial to enable the widespread adoption of composite scintillators for efficient radiation detection applications. Ball milling presents a scalable method for synthesizing perovskite nanocrystals and polycrystalline powders, facilitating large-scale production.

Ball milling is a mechanical grinding process that can be performed either dry or wet. This method involves rotating a bowl containing the material and grinding balls, the mechanical energy is provided by the rotary motion of the bowl and involves friction between the grinding medium (balls) and the material being ground. Both the container and the balls are usually made of hard materials like zirconia, corundum, or stainless steel. The milling process can reduce particle size to the nanometre scale, mix materials efficiently, and induce solid-state chemical transformations. While it has been successfully used for producing metal oxide nanoparticles[116] and alloyed materials,[117] ball milling faces challenges with semiconductor nanocrystals due to structural defects and inadequate surface passivation, leading to low photoluminescence quantum yields. However, recent progress has been made in using ball milling for the synthesis of perovskites, showing promise in improving their structural stability and photoluminescent properties.[118,119]

In 2023, Ghosh *et al.* reported a room temperature, scalable mechanochemical synthesis method using the ball milling technique without using any toxic and volatile solvents.[90] They used zirconium oxide balls in a zirconium oxide jar to mill a mixture of CsBr and $PbBr_2$, followed by the addition of the ligand oleylamine (Fig. 2c). The resulting product was dispersed in toluene, and after settling, the colloidal dispersion of $CsPbBr_3$ perovskite NCs was obtained for further use. The $CsPbBr_3$ NCs thus synthesized were reported to have a PLQY of 88% after surface modification of the NCs using the surfactant oleylamine. The $CsPbBr_3$ synthesized using this solvent free method was used to fabricate $CsPbBr_3$–PMMA composites. After 60 days of water storage under UV illumination, no visible drop in the fluorescence was observed for these composites. The stability could be potentially attributed to the solvent free synthesis method of the nanocrystals. Ball milling has also been reported for lead free metal halides.[120] Li *et al.* utilized the ball-milling technique to synthesize the copper-based metal halide $Cs_3Cu_2I_5$. Initially, CsI and CuI powders, with a molar ratio of 3 : 2, were placed into a steel jar and subjected to ball milling for a duration of several minutes. The ball milled $Cs_3Cu_2I_5$ powder demonstrated a PLQY of 74.5% and the XRD peaks of the milled sample was matched with the orthorhombic phase of $Cs_3Cu_2I_5$.

The ball milling method's capacity for large-scale production, makes this approach particularly attractive for scaling up metal halide polymer composites for scintillator applications. Despite these advantages, challenges such as achieving uniform particle size and properties, as well as potential contamination from the milling media, need to be addressed to fully realize the method's potential.

4.2 Perovskite polymer composites

In this section, we will explore various methods commonly employed in the creation of perovskite–polymer composites tailored for scintillator applications. These techniques include dispersing perovskite NCs into polymer precursors, solution blending of perovskite precursor and polymer precursors, employing an *in situ* approach, and utilizing radical polymerization.[121,122] Each method offers unique advantages and challenges, contributing to the optimization of composite properties and the enhancement of scintillation performance. Through an examination of these fabrication methodologies, we aim to elucidate the diverse strategies available for fabricating efficient and versatile perovskite–polymer composites suitable for radiation detection and imaging applications.

4.2.1 Dispersion of perovskite nanocrystals into polymer precursor. One common method for fabricating perovskite–polymer composites involves the dispersion of perovskite NCs into polymer precursors. Here, the perovskite NCs could also be in the colloidal solution form. In this approach, perovskite NCs, typically synthesized separately, are dispersed, or mixed into a solution containing the polymer precursor. This mixture is then subjected to various processing techniques such as stirring, sonication, or mechanical mixing to ensure homogenous dispersion of the perovskite NCs within the polymer matrix. Once dispersed, the composite solution can be deposited onto a substrate using methods like spin coating, blade coating, or drop casting. Subsequent curing or solidification results in the formation of the final composite material.

Several groups have reported the fabrication of perovskite polymer composites using these techniques for scintillator applications. The choice of polymer, along with the solvent, is crucial for achieving uniform dispersion of perovskite NCs within the polymer matrix. Solvents with suitable evaporation rates, compatibility with the chosen polymer, and appropriate polarity ensure proper distribution of the NCs throughout the bulk of the composite structure. Different kinds of polymers

have been used to make the perovskite–polymer composites using this method. Polymethyl methacrylate (PMMA), due to its high transparency, flexibility and good thermal stability has been reported by several groups. Furthermore, its hydrophobic nature can also protect the perovskites from potential degradation resulting from exposure to air or moisture in the surroundings. A $CsPbBr_3$–PMMA composite was reported by Wang *et al.*[80] The $CsPbBr_3$ perovskite NCs, synthesized using the hot-injection method, were dispersed in a PMMA-toluene solution. The thickness of the film is controlled by the amount of polymer precursor that is added to the mixture. Later, the perovskite polymer mixture is poured into a template for annealing (Fig. 3a). In the case of single crystal metal halides, they are first ground into smaller sized particles before being blended into the polymer precursor solution, to achieve a more uniform dispersion of the crystalline material within the polymer matrix. Several other groups have also reported the use of PMMA for their perovskite polymer composites for scintillator applications.[110,112,123] A similar procedure using chloroform as the solvent for the PMMA polymer precursor was also reported.[81,105,109] In addition to PMMA, polydimethylsiloxane (PDMS) is also frequently utilized in scintillator perovskite polymer composites owing to its advantageous properties. It offers notable benefits such as excellent thermal

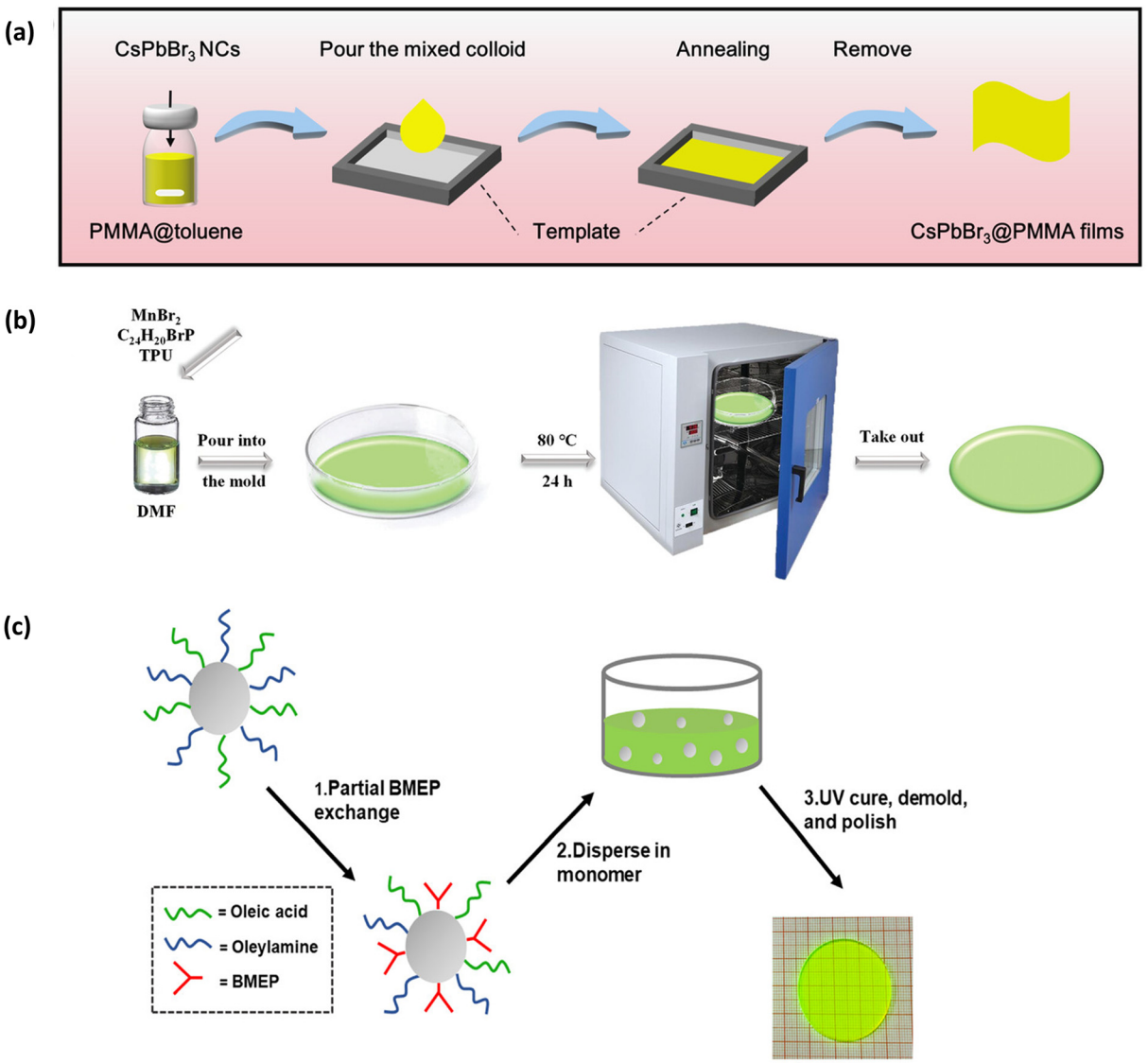

Fig. 3 Synthesis methods for the perovskite–polymer composites. (a) A schematic diagram of the template assisted method for the synthesis of the $CsPbBr_3$-polymethylmethaceylate (PMMA) composite films. The nanocrystals are first dispersed into the polymer precursor solution and then poured into the template for solvent evaporation. Reproduced with permission from ref. 80. Copyright 2022 John Wiley and Sons. (b) *In situ*-method for the fabrication of $(C_{24}H_{20}P)_2MnBr_4$-thermoplastic polyurethane (TPU) scintillation film. Reproduced with permission from ref. 130. Copyright 2022 John Wiley and Sons. (c) A schematic illustration for the fabrication of $CsPbBr_3$-polybutylmethacrylate (PBMA) nanocomposites using the radical polymerization method. The organic ligands added to the nanocrystals are also shown. Reproduced with permission from ref. 98. Copyright 2021 American Chemical Society.

stability, flexibility and optical transparency. Zhang *et al.* reported PDMS-Cs_2ZrCl_6 composites for scintillator applications.[107] The Cs_2ZrCl_6 powder, synthesized using the acid precipitation method, was mixed with PDMS at a 1 : 2 mass ratio, degassed, drop-cast onto a glass substrate, and spin-coated to form uniform films. After curing at 120 °C for 20 minutes, the films were cooled and peeled off. The thickness of the film was controlled by the number of spin-coatings. A similar procedure using PDMS was reported by several other groups.[92,101,103,104,113,114,120,124]

In this method when the prepared perovskite NCs are mixed into the polymer precursor solutions, it can often lead to issues such as powder agglomeration and reduced transparency of the scintillation films. Zhou *et al.* reported the addition of a ligand, ethyl acetate, to the $Cs_3Cu_2I_5$ particle-PDMS mixture to mitigate the aggregation of $Cs_3Cu_2I_5$ particles and to improve the film morphology.[100] It was shown that the film without the addition of ethyl acetate exhibited poor surface morphology due to the aggregation of $Cs_3Cu_2I_5$ particles. In addition to these polymers, another commonly used polymer is polystyrene. Although its thermal stability and transparency may be inferior to PMMA and PDMS, polystyrene offers the advantages of good optical clarity, cost-effectiveness, and reasonably good radiation hardness.[125] Han *et al.* reported the fabrication of $Cs_3Cu_2Cl_5$-polysterene composites for scintillator applications. $Cs_3Cu_2Cl_5$:2%K+ powders were dissolved in toluene, followed by the addition of polystyrene solution. The mixture was cast into a mold and air-dried to produce a thin film. Several other groups have also reported the use of polystyrene to make composites for scintillator applications.[78,82,84,102,111,126] Another approach, based on a suction filtration technique, to avoid aggregation, was reported by Wu *et al.* to produce scintillator films.[83] Initially, a solution containing perovskite NCs of Ce^{3+} ion doped $CsPbBr_3$, synthesized using the hot-injection method, was filtered through a polyvinylidene fluoride (PVDF) film using a vacuum pump, resulting in a uniform scintillator layer with high density and ultra-thin thickness (30 μm) on the surface of the PVDF film. Subsequently, a layer of polystyrene (PS) was applied to cover the scintillator layer, filling any gaps between the scintillator particles. This facilitated the easy transfer of the scintillator film onto an ultra-thin quartz sheet. The suction filtration method was compared to the conventional spin-coating approach and yielded scintillator films with smoother surfaces, denser layers, and higher transparency. Additionally, it enabled the production of large-area scintillator films, which could be tailored into different shapes to meet specific needs, showcasing potential for high-resolution X-ray microscopic imaging.

4.2.2 *In situ* method. The *in situ* method of polymer-perovskite precursor solution blending involves the simultaneous mixing of perovskite precursor solutions with polymer precursors. This blending occurs during the preparation process, allowing for the direct incorporation of perovskite NCs into the polymer matrix. By combining the two precursors *in situ*, this method eliminates the need for separate perovskite NC synthesis, thereby simplifying the composite fabrication process. However, this approach initially led to phase separation between the perovskite and the polymer matrix, resulting in aggregated perovskite particles with low PLQY.[127] Zhong *et al.* addressed this issue by developing a controlled drying process using PVDF as the polymer matrix. This method produced composite films with uniformly sized and spatially distributed perovskite NCs, achieving high PLQY (>90%).[128,129]

This *in situ* method has also been adopted by several groups for scintillator applications. Chen *et al.* reported an *in situ* strategy to minimize the aggregation of the $CsPbBr_3$ perovskite NCs by using a highly viscosity polymer like PMMA for composite film fabrication.[131] The high viscosity environment slows down the movement of atoms and perovskite NCs, preventing rapid migration before the film solidifies, leading to a more uniform distribution of the perovskite NCs and potentially avoiding issues such as agglomeration and Ostwald ripening. The *in situ* method showed better performance when compared with the mixing method where pre-formed perovskite NCs are mixed with the polymer precursors to form the composites. Xia *et al.* reported the use of this *in situ* method for lead free Mn-based perovskite scintillator films.[130] In this method, the Mn-based perovskite precursor powders, $MnBr_2$, $C_{24}H_{20}BrP$ and the thermoplastic polyurethane (TPU) powders were dissolved in *N*,*N*-dimethylformamide (DMF), followed by solvent evaporation (Fig. 3b). The perovskite polymer composite films of $(C_{24}H_{20}P)_2MnBr_4$-TPU prepared using the *in situ* method have an emission at 520 nm with a stable peak intensity from 20 °C to 150 °C. Even after six months of ambient storage, the film's initial photoluminescence intensity remained intact, highlighting TPU's role in improving the scintillator film's environmental stability. In addition, one of the aims of employing the *in situ* method is to address aggregation issues and to enhance the transmittance of the scintillator films. The scintillator films fabricated with the *in situ* method showed a 70% transmittance at a thickness of 110 μm, which however decreased to approximately 50% at 360 μm thickness.

The *in situ* method was also reported for lead free inorganic copper based metal halide $Cs_3Cu_2I_5$ scintillator films.[132] A solution containing cesium iodide (CsI), copper iodide (CuI), phosphinic acid (H_3PO_2) and PMMA in DMF was deposited on a glass substrate through blade coating with subsequent solvent evaporation. Phosphinic acid was added to the solution mixture to prevent oxidation of the copper ion. The composite films prepared have a PLQY of 78.42% which increased to 97.53% after 0.1% Thallium doping. The *in situ* method has also been investigated for composites with lead free organic copper-based metal halides like $(TBA)CuX_2$ (TBA = tetrabutylammonium; X = Br, Cl).[115]

In the two methods discussed above, the perovskite–polymer mixture is cast onto a substrate followed by solvent evaporation. Methods like spin coating, drop casting and blade coating, commonly used to deposit the mixture onto the substrate, are not favourable methods in terms of scalability due to their limited throughput. These methods are typically capable of coating only small areas at a time, leading to

increased processing time and cost. Also, one of the significant challenges associated with these techniques is achieving uniformity across large areas. In addition, methods like spin coating also lead to material waste. The excess solution spun off during the spin coating process results in significant wastage, especially when dealing with larger substrates. This inefficiency in material usage becomes more pronounced as the scale of production increases. Furthermore, the equipment employed for spin coating and blade coating may not be readily scalable to accommodate larger substrates. Upgrading or replacing such equipment to handle larger volumes typically entails considerable costs and may necessitate extensive modifications to ensure compatibility with the increased scale of production.

4.2.3 Radical polymerization. In the dispersion methods discussed so far, where perovskite NCs or their colloidal solutions are mixed with polymer precursors, ensuring complete polymerization to minimize residual monomer content can be challenging. Residual monomer refers to the unreacted starting material remaining after the polymerization process of a polymer. The amount of residual monomer after polymerization can influence the composite properties and stability, potentially compromising chemical stability and mechanical strength.[133] Radical polymerization is a method where monomers are polymerized into a polymer chain in the presence of a radical initiator. In this method, the polymerization is initiated through the generation of free radicals, which are highly reactive species capable of initiating polymer chain growth. The method of radical polymerization, commonly used in plastic scintillators to reduce residual monomer content, can also benefit perovskite polymer composites.

In the case of perovskite–polymer composites, this method involves incorporating perovskite nanoparticles or precursors into the monomer mixture before initiating polymerization. This method was reported by Nie *et al.* for the fabrication of $CsPbBr_3$-polybutylmethacrylate (PBMA) composites.[98] In this method, the $CsPbBr_3$ NCs, synthesized using a modified precipitation method, were introduced into 10 mL of butyl methacrylate (BMA) solution along with ethylene dimethacrylate (EDMA) and diphenyl(2,4,6-trimethylbenzoyl) phosphine oxide (TPO). The mixture underwent sonication for 30 minutes. Prior to use, both BMA and EDMA underwent purification using basic alumina to eliminate inhibitors. The solution was then transferred to a flat-bottom glass vial and sealed under nitrogen protection. Polymerization was initiated by exposing the mixture to a UV lamp (365 nm) for 12 hours (Fig. 3c). Here, the TPO acts as the photo initiator and absorbs the UV light and generates free radicals capable of initiating polymerization. Following curing, the resulting composite was demoulded from the glass vial. This process can help minimize residual monomer content in perovskite–polymer composites. However, the initiators used in radical polymerization, such as TPO in the described process, could interact with perovskites. These interactions can potentially affect the stability and optical properties of the perovskite NCs, limiting the applicability of the process.

5. Metal halide perovskite composites for indirect X-ray detection

In this section, we will discuss three distinct categories of perovskite/metal halide structures that have been utilized in scintillator applications. These categories include lead-based 3D perovskites, 2D and lower-dimensional lead-based perovskites, and lead-free perovskites/metal halides. The classifications are rooted in the crystal structure of the materials, with their dimensionality serving as the primary distinguishing factor.

5.1 3D Lead-based metal halide perovskite composites

3D lead-based metal halide perovskites are emerging as promising materials for X-ray scintillation. Among these, inorganic perovskite compounds like $CsPbBr_3$,[134,135] alongside organic–inorganic hybrids like $MAPbBr_3$ and $FAPbBr_3$,[136] show prominent scintillation performance. The challenge for using these materials as scintillators lies in their susceptibility to degradation from environmental factors like moisture, heat, photodegradation, compromising their long-term performance. In addition, ensuring stability under X-ray irradiation is also crucial for maintaining the integrity and effectiveness of these materials over extended periods of use. 3D perovskite polymer composites hold promise in addressing these challenges, offering enhanced stability against environmental factors such as moisture, heat, and irradiation (Table 1). Researchers have explored various strategies to improve the stability of these composites under X-ray irradiation, focusing on compositional engineering and structural modifications to enhance their performance and reliability over time.

In 2020, Cao *et al.* used the "emitter-in matrix" design to embed $CsPbBr_3$ NCs inside a Cs_4PbBr_6 crystal matrix to enhance the irradiation stability of the pure $CsPbBr_3$ NCs.[99] The $CsPbBr_3$@Cs_4PbBr_6 system was synthesized using the anti-solvent method. After a 4-hour 30 W UV irradiation stability test of the pure $CsPbBr_3$ NCs and the $CsPbBr_3$@Cs_4PbBr_6 system, the $CsPbBr_3$@Cs_4PbBr_6 system showed almost no degradation while the pure $CsPbBr_3$ NCs retained only 53% of its emission intensity and showed signs of light induced aggregation. To further enhance the stability of the emitter-in matrix" design and to test its X-ray imaging capabilities, a $CsPbBr_3$@Cs_4PbBr_6-polystyrene composite was fabricated. The composite film was fabricated by the dispersion of the $CsPbBr_3$@Cs_4PbBr_6 powder into the polystyrene polymer precursor solution. X-ray images captured using the composite were comparable to that obtained using the commercial scintillator CsI:Tl. However, in this kind of a "emitter-in-matrix" design structure, there are debates on whether the bright green emission observed in $CsPbBr_3$@Cs_4PbBr_6 originates from Cs_4PbBr_6 itself, potentially through midgap defect centers or self-trapped excitons, or from the embedded $CsPbBr_3$ NCs that are challenging to identify using conventional methods such as X-ray diffraction (XRD) and transmission electron microscopy (TEM).[137,138] In this work, to address

Table 1 Scintillation properties of lead based metal halide perovskites and their polymer composites

Material	Synthesis method of emitter	Synthesis method of composite/film: polymer	Emission (nm)	Light Yield (photons/MeV); method used	Detection limit (nGy s^{-1})	Spatial resolution (lp mm^{-1} or μm)	Decay time (ns)	Radiation Hardness (Residual RL %; dose (Gy))	Ref.
$CsPbBr_3$	*In situ*	*In situ*: PMMA	515	15 800; comparison	120	12.5			131
$CsPbBr_3$	Hot injection	Dispersion: PMMA	532		40.1 (SNR = 3)	8.5	8.25	>97%; 2.1384	80
$CsPbBr_3$ QDs	Commercial	Dispersion: polystyrene	530	2900; pulse height spectra					139
$CsPbBr_3$	LARP	Dispersion: PMMA	518	9000; comparison			3.4	>85%; 800	108
$CsPbBr_3$ nanosheets	Hot injection (modified)	Dispersion: PMMA	510		38.7	135 μm		~90%; 0.521	81
$CsPbBr_3$	Precipitation (modified)	Radical polymerization: PBMA	515		4600		13		98
$CsPbBr_3$	Hot injection	Dispersion: polystyrene	533				1.5		78
$CsPbBr_3$	Hot injection	Dispersion: spray coated on paper/PMMA	533	30 000; comparison	2971 (SNR = 3)	5	35	97%; 103.536	79
$CsPbBr_3$	Ball milling	Dispersion: PMMA	536			8	29.4		90
$CsPbBr_3$	LARP	Dispersion: PMMA	520	860; pulse height spectra			2		109
$CsPbBr_3$	Commercial	Dispersion: resin	534	21 500; pulse height spectra		4 (MTF = 0.2)	10.5		140
$FAPbBr_3$	LARP	Dispersion: PMMA	531	33 000; comparison			62		110
8%Ce^{3+}:$CsPbBr_3$	Hot injection	Suction filtration: PVDF	530	33 000; comparison		580 (MTF = 0.2)	7.09	~97%; 4.8	83
$(C_{12}H_{25}NH_3)_2PbBr_4$:$Mn^{2+}$	Acid precipitation	Dispersion: PMMA	620	35 292; comparison	108 170 (SNR = 3)	10		89.5%; 152.14 @90 keV	105
$(C_4H_9NH_3)_2PbBr_4$:10% Mn^{2+}	Acid precipitation	Dispersion: PMMA	610	85 000; comparison	16 (SNR = 3)	10.7			106
$CsPbBr_3$@Cs_4PbBr_6	Antisolvent	Dispersion: polystyrene	520	6000; comparison			3		99
$CsPbBr_3$@PbBrOH	Precipitation	Dispersion: polystyrene	520		4000			~90%; 0.338	126
$CsPbBr_3$@$CsPb_2Br_5$	Hot injection	Dispersion: polystyrene	522	19 200; comparison	1130	8.19 (MTF = 0.2)	2.93	94%; 10.8	82

these concerns, a neutron scattering technique was employed to validate the existence of $CsPbBr_3$ NCs within the Cs_4PbBr_6 host.

A "emitter in matrix" design was also reported by Guo *et al.* by incorporating highly luminescent 3D $CsPbBr_3$ NCs into a 1D PbBrOH matrix.[126] The incorporation of the 1D PbBrOH matrix was found to enhance the stability of the $CsPbBr_3$ NCs. The $CsPbBr_3$@PbBrOH powders were synthesized using a precipitation method. The integrated photoluminescence intensity of $CsPbBr_3$@PbBrOH powders remained around 80% after exposure to air for 120 days. The presence of the heavy Pb atom in the 1D PbBrOH matrix was also found to enhance the X-ray absorption coefficient of $CsPbBr_3$@PbBrOH compared to the $CsPbBr_3$ NCs in the 0.1–1 MeV range. The $CsPbBr_3$@PbBrOH-polysterene composite films were prepared by the dispersion of the $CsPbBr_3$@PbBrOH powder into the polystyrene polymer precursor solution, at a fabrication cost of $1.5 per g, which was shown to be cheaper than that of commercial scintillators like BGO and CsI : TI. A similar "emitter in matrix" design of a dual-phase $CsPbBr_3$–$CsPb_2Br_5$ perovskite NC was reported by V. Naresh *et al.* for scintillator applications.[82] Here, the $CsPbBr_3$–$CsPb_2Br_5$ scintillator films were fabricated by dispersing the $CsPbBr_3$–$CsPb_2Br_5$ perovskite NCs into the polystyrene polymer precursor solution.

Under X-ray radiation exposure, perovskite NCs experience damage that leads to aggregation, compromising their optical and structural properties. Despite their susceptibility to damage, it has been reported that damaged polymer nanocomposites retain the potential for recovery through post-annealing treatments. An annealing treatment to recover the damaged perovskite polymer composite after long term exposure to X-ray irradiation was reported by Chen *et al.*[131] In this work, the $CsPbBr_3$ NCs were synthesized using the hot injection method and the $CsPbBr_3$–PMMA composites were made using the *in situ* method. After subjecting the damaged perovskite scintillator to thermal treatment at 80 °C for 4 hours, it was observed that the composites underwent full recovery (Fig. 4(a–c)). The radioluminescence (RL) of the composite films could be restored to its initial level even after undergoing 50 such cycles of damage and recovery.

In addition to stability, another attribute that is beneficial for X-ray imaging using perovskite–polymer scintillators is their flexibility, enabling the imaging of non-flat objects with higher accuracy. This flexibility is a distinct advantage offered by perovskite–polymer scintillators compared to other single crystal scintillators. Wang *et al.* reported a template assembled method to fabricate $CsPbBr_3$–PMMA composites.[80] The composite film was fabricated by the dispersion of the $CsPbBr_3$ NCs into the PMMA polymer precursor solution. To verify the bending stability of the $CsPbBr_3$-PMMA composites, the photoluminescence (PL) intensity was measured after 2000 bending cycles. Almost 94% of the initial PL intensity was measured, showcasing good bending stability. Further, the luminescence after exposure to water was measured for both pure $CsPbBr_3$ NCs and the $CsPbBr_3$–PMMA composites. The pure $CsPbBr_3$ NCs maintain only 28% of their initial luminescence after

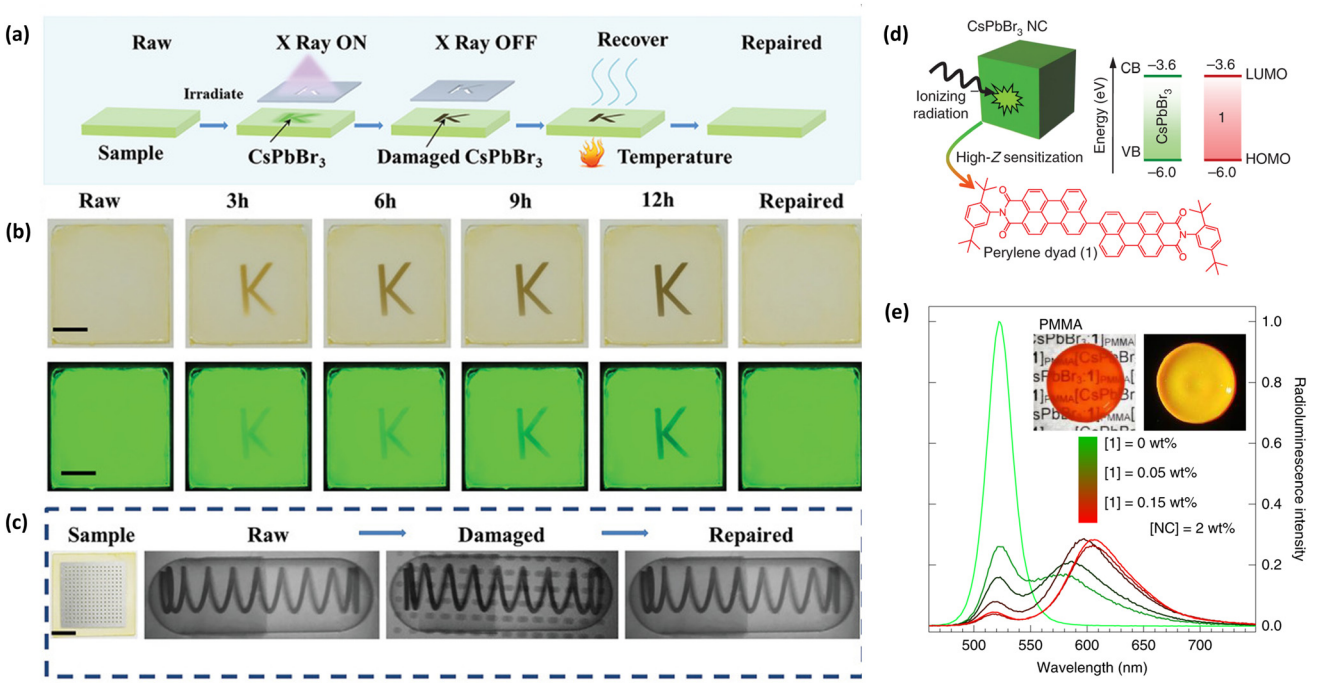

Fig. 4 Irradiation stability and self-absorption in 3D lead based metal halide perovskites. (a) A schematic diagram for repairing the damage in the perovskite polymer composite films after X-ray irradiation *via* a thermal treatment (b) the damaged composite film after different durations of the X-ray irradiation and on the far right, the repaired film after thermal treatment under natural (upper row) and UV illumination (bottom row). The film was used to image a mask with a letter K. (c) X-ray images obtained using the composite films under three conditions, raw (before X-ray irradiation), damaged (after 12 hours of X-ray irradiation) and repaired (after the damaged composite film is repaired through a thermal treatment). Reproduced with permission from ref. 131. Copyright 2021 John Wiley and Sons. (d) Schematic of the $CsPbBr_3$ NCs sensitizing the organic dye. An energy diagram showing the resonance between the highest occupied molecular orbital (HOMO) and the lowest unoccupied molecular orbital (LUMO) energy levels of the $CsPbBr_3$ NCs and the organic dye. (e) The radioluminescence spectra of the $CsPbBr_3$–PMMA nanocomposites. The weight percentage of the organic dye (represented as ref. 1) in the composites is increased from 0 to 0.15%. Inset: photographs of the PMMA nanocomposites under ambient light (left) and under 400 nm light (right). Reproduced with permission from ref. 108. Copyright 2020 Springer Nature.

72 hours in water. In contrast, $CsPbBr_3$@PMMA films retain 81% of their initial luminescence after 2520 hours in water.

This demonstrated the enhanced stability of the $CsPbBr_3$–PMMA composites against water and oxygen damage.

Traditional organic plastic scintillator materials, while offering fast responsivity, suffer from low interaction probability with high-energy photons due to their low effective atomic number. This limitation can be addressed by loading luminescent nanoparticles like perovskites with heavy metal elements into plastic scintillators. Magi *et al.*, reported a method to incorporate metal halide perovskite quantum dots (QDs), into plastic scintillators.[139] The composites were fabricated by dispersing the commercial perovskite quantum dots into the polymer precursor solution of polystyrene and 2-(4-*tert*-butylphenyl)-5-(4-phenylphenyl)-1,3,4-oxadiazole (*b*-PBD) in tetrahydrofuran (THF). This fabrication process resulted in opaque, crack-free scintillators with colours derived from the perovskite quantum dots. The detection efficiency for 67.4 keV X-rays was successfully enhanced by loading the perovskite quantum dots. The scintillation light yield was measured using the pulse height spectra method. The composites loaded with the green $CsPbBr_3$ quantum dots showed a light yield of 2900 photons per MeV. However, it was observed that the scintillation light yields were lower than the composites loaded with non-emissive nanoparticles, like hafnium dioxide (HfO_2) or bismuth trioxide (Bi_2O_3), possibly due to self-absorption of the QD emission. Therefore, the study concluded that optimizing the concentration of perovskite QDs to minimize self-absorption is crucial for fully exploiting their excellent emission properties and maximizing the detection efficiency of X-rays in plastic scintillators.

Self-absorption is a phenomenon where the photons emitted by a material after the absorption of incident radiation is reabsorbed by the material itself. In perovskite–polymer composite scintillators, self-absorption results in a reduction of the efficiency of the scintillator material. A common strategy to prevent self-absorption is to incorporate a dye/chromophore that has an absorption peak that overlaps the emission of the perovskite NCs in the composite. In 2020, Gandini *et al.* addressed this issue by incorporating an organic molecule perylene dyad 9,9′-bis[perylene-3,4-dicarboxylic-3,4-(*N*-(2,5-di-*tert*-butylphenyl))] into $CsPbBr_3$–PMMA nanocomposites.[108] The highest occupied molecular orbital (HOMO) and lowest unoccupied molecular orbital (LUMO) levels of the organic emitter aligned precisely with the conduction bands of $CsPbBr_3$ NCs, ensuring efficient energy transfer (Fig. 4d). In this work, the

$CsPbBr_3$ NCs were synthesized using the LARP method and the $CsPbBr_3$–PMMA composites were fabricated by dispersing the $CsPbBr_3$ NCs into the PMMA polymer precursor solution. In the radioluminescence (RL) spectra of the NC-PMMA nanocomposites, the RL of the pure nanocrystals gradually diminishes with increasing loads of the organic dye, favouring the emission from the organic dye (Fig. 4e). To further validate this strategy, a 300 μm thick layer of the PMMA nanocomposite was used as the active layer atop an optical-grade PMMA waveguides with dimensions of 0.5 cm × 0.7 cm × 15 cm. The integrated RL intensity of the spectra collected at the waveguide edge shows only a slight decrease of ~25%, attributed to reabsorption over about 12 cm, suggesting that the emission of the organic dye was preserved. In addition to minimal reabsorption losses, the composites also showed a short decay time of 3.4 ns. The light yield of the composite was estimated to be ~9000 photons per MeV using the comparison method, using Bismuth Germanate (BGO) and a commercial plastic scintillator (Kuraray SCSF-3HF) as the reference.

The issue of self-absorption in 3D perovskite nanosheets was addressed by Wang *et al.*[81] $CsPbBr_3$ nanosheets, synthesized using a modified hot injection method, were used as the X-ray absorber. For the interfacial energy transfer, an organic chromophore difluoroboron 1,3-diphenylamine β-diketonate (A) with thermally activated delayed fluorescence (TADF) was chosen to be incorporated into the $CsPbBr_3$–PMMA composites. The composites were fabricated by mixing the $CsPbBr_3$ nanosheets with the PMMA polymer precursor solution. The energy transfer efficiency from the perovskites to the organic chromophore was calculated to be more than 90%. The nanocomposite scintillator film exhibited good photostability and retained 90% of the initial RL value after a total irradiation dose of 0.521 Gy. The composites demonstrated a 135 μm imaging resolution and a low detection limit of 38.7 nGy s^{-1} (Table 1). This X-ray imaging resolution was reported to be higher than its perovskite nanosheet counterparts. This detection limit is 142 times lower than the dose typically used in X-ray medical imaging.

In perovskite–polymer composites, it is crucial that the composites are transparent to the specific wavelength emitted by the perovskite to achieve optimal performance. Therefore, ensuring homogeneity and preventing the aggregation of perovskite NCs within the composite is essential. Surface modification of the perovskite NCs with ligands is a strategy employed to alleviate their aggregation, minimizing scattering effects and enhancing the overall performance of the composite. Nie *et al.* reported a surface modification method using a long chain ligand, bis(2-(methacryloyloxy)ethyl) phosphate (BMEP), instead of the commonly reported short chain ligands like oleylamine and oleic acid, to reduce the aggregation of the $CsPbBr_3$ NCs embedded in the polybutylmethacrylate (PBMA) composites.[98] Here, the $CsPbBr_3$ NCs were synthesized using a modified precipitation method and the $CsPbBr_3$-PBMA composites were fabricated using the radical polymerization method. The optical enhancement using this method was verified by the improvement in transmittance in the visible range in the BMEP-treated $CsPbBr_3$/PBMA composites compared to the as-grown $CsPbBr_3$/PBMA composites. As the concentration of the embedded $CsPbBr_3$ NCs increases in the BMEP-treated $CsPbBr_3$/PBMA composites, their photoluminescence (PL) intensity shows enhancement. Despite this, the transparency of the composites decreases slightly with higher NC concentrations. However, even with a concentration of 0.06 wt% NCs, the composites retain more than 50% transmittance within the wavelength range of 530–800 nm. The distinct absorption edge around 505 nm is attributed to the $CsPbBr_3$ NCs (Fig. 5a and b).

Surface modification strategy using the ligand Bis(2-(methacryloyloxy)ethyl) phosphate(BMEP) was also reported by Braddock *et al.* for formamidinium lead bromide ($FAPbBr_3$) perovskite NCs.[110] The $FAPbBr_3$ perovskite NCs were synthesized using the LARP method and the $FAPbBr_3$-PMMA composites were fabricated by dispersing the $FAPbBr_3$ NCs in the PMMA polymer precursor solution. The surface modification using BMEP was shown to improve the light transmission through the $FAPbBr_3$-PMMA composites. In addition to BMEP, other surface ligands have also been explored. Děcká *et al.* reported the surface modification of the $CsPbBr_3$ NCs in a polystyrene matrix using didodecyldimethylammonium bromide (DDAB).[78] The $CsPbBr_3$ NCs were synthesized using the hot injection method and the $CsPbBr_3$-polystyrene composite was fabricated by mixing the $CsPbBr_3$ colloidal solution with the polystyrene polymer precursor solution. DDAB demonstrated superior surface passivation capability when compared to the conventional combination of oleic acid (OA) and oleylamine (OAm). The $CsPbBr_3$-polystyrene composite coated with OA and OAm exhibits 50% transmittance at 800 nm. In contrast, the nanocomposite coated with dodecylammonium bromide (DDAB) shows an improved transmittance of 56% at the same wavelength.

In addition to strategies to reduce aggregation of the NCs, synthesis methods that minimize the use of toxic solvents have also been investigated. A solvent free approach to synthesize $CsPbBr_3$ NCs and fabricate $CsPbBr_3$–PMMA composites was reported by Ghosh *et al.*[90] The $CsPbBr_3$ NCs were synthesized using the ball milling method and the $CsPbBr_3$-PMMA composites were fabricated by dispersing the $CsPbBr_3$ NCs in the PMMA polymer precursor. The composites had the radioluminescence (RL) emission peak at 536 nm with an FWHM of approximately 16 nm.

In medical X-ray imaging, the risk of exposure to high radiation raises safety concerns for patients. Thus, real time monitoring of the radiation dose is crucial. Current scintillators used for radiation detection are bulky and expensive, which make them an unsuitable option to be worn on the body for personal safety. Chen *et al.* reported a spray coating method to fabricate flexible, large area and low-cost X-ray imaging screens with a visible dose rate indicator.[79] The $CsPbBr_3$ NCs synthesized using the hot injection method, are spray coated on a paper substrate, followed by a thin layer of PMMA. The protective layer of PMMA, prevents the degradation of the perovskite NCs during prolonged exposure to environmental con-

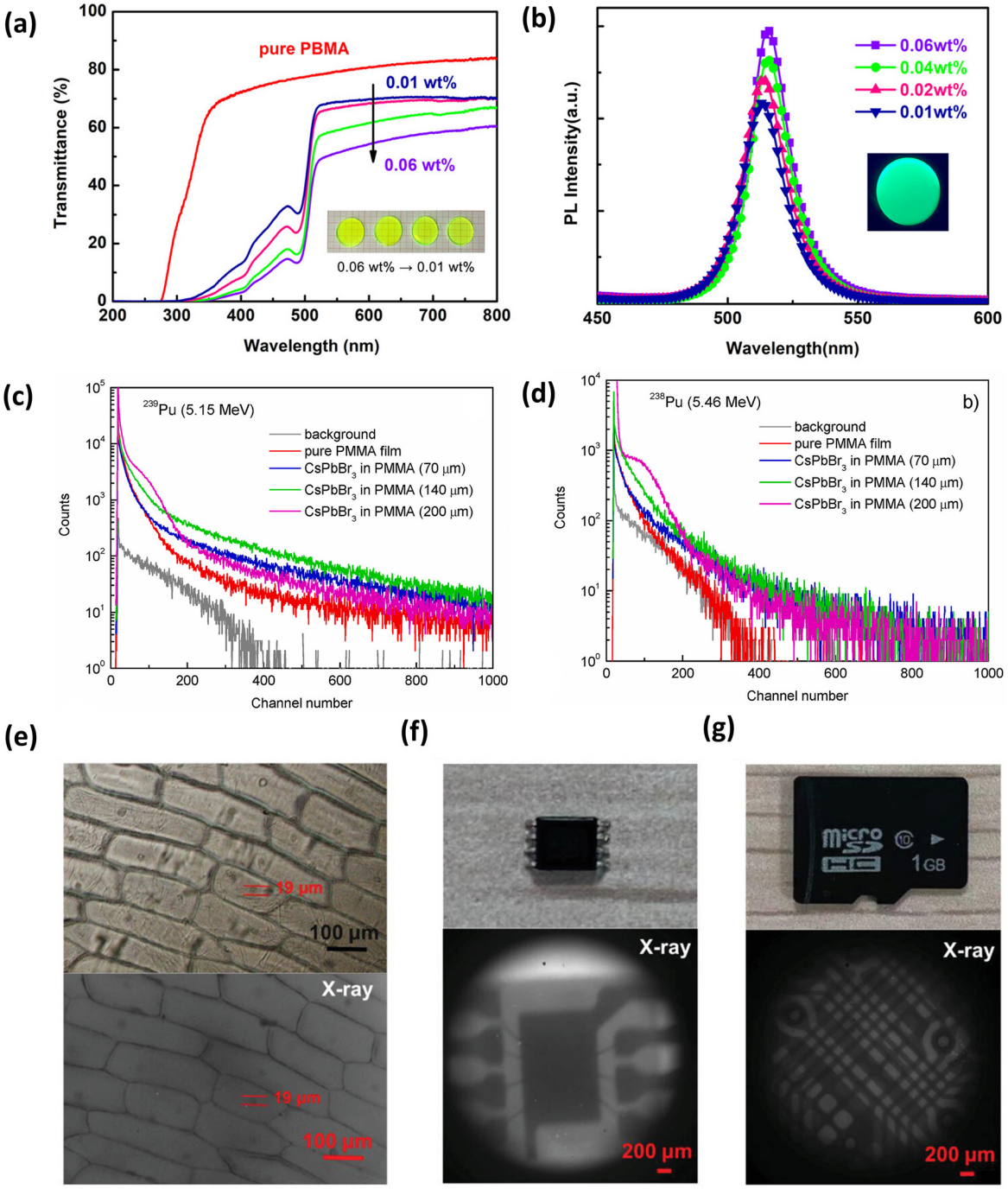

Fig. 5 Properties of 3D lead based metal halide perovskite polymer composites. (a) Transmittance spectrum of the bis(2-(methacryloyloxy)ethyl) phosphate (BMEP) treated $CsPbBr_3$-polybutylmethacrylate (PBMA) composites. As the weight percentage of the loaded nanocrystals in the composite increases, the transmittance of the composites decreases. The inset shows the photographs of the BMEP treated $CsPbBr_3$-PBMA composites for the different weight percentages. (b) The photoluminescence (PL) spectra of the $CsPbBr_3$-PBMA composites, the PL intensity increases with the weight percentage of the loaded nanocrystals. The inset shows the photographs of the $CsPbBr_3$-PBMA composites under 365 nm UV illumination. Reproduced with permission from ref. 98. Copyright 2021 American Chemical Society. Pulse height spectra of the $CsPbBr_3$–PMMA films with varying thickness when exposed to α-particles emitted by (c) ^{239}Pu and (d) ^{238}Pu sources. Reproduced with permission from ref. 109. Copyright 2023 Elsevier. Application of the scintillator films in X-ray imaging in diverse fields like biology and microelectronics. (e) Top images show onion epidermal cells treated with potassium iodide iodine solution, while the bottom images depict their X-ray image captured using the scintillator film. (f) The upper photos display a chip; the bottom image is its X-ray image captured using the scintillator film. (g) The upper picture shows a storage card, and the bottom is its X-ray image captured using the scintillator film. Reproduced with permission from ref. 83. Copyright 2022 John Wiley and Sons.

ditions. No significant deterioration was observed after 2000 hours of storage in water and air for over 300 days. The light yield of the film was estimated to be ~30 000 photons per MeV using the comparison method, using a commercial CsI:Tl crystal scintillator as the reference. A proof-of-concept prototype in a "WIFI" logo shape was created for a real-time dose rate indicator using $CsPb_xMn_{1-x}Cl_3$ perovskite NCs (MH-NCs), where luminescent properties were tuned by adjusting the Mn^{2+} content. The design ensured that as the dose rate increased, more arcs got illuminated, enabling dose rate estimation by counting the number of illuminated arcs.

In most studies on perovskite polymer composite scintillators, the comparison method has been used to measure the light yield. However, the light yield measurement using the pulse height spectra method was reported by Skrypnyk *et al.* for $CsPbBr_3$–PMMA composites.[109] Here, the $CsPbBr_3$ perovskite NCs were synthesized using the LARP method and the $CsPbBr_3$–PMMA composites were fabricated by mixing the $CsPbBr_3$ colloidal solution with the polystyrene polymer precursor solution. The pulse height spectra of the composite films were measured upon excitation by α-radiation of radionuclides ^{239}Pu (E_α = 5.15 MeV) and ^{238}Pu (E_α = 5.46 MeV) (Fig. 5c and d). The light yield for the 200-μm thick composite film was measured to be 860 photons per MeV, which is lower than that reported in other similar studies. The authors report that the light yield can be further improved by tuning the concentration of the NCs and the film thickness. The light yield using the pulse height spectra method was also reported by Maddalena *et al.*[140] Commercial $CsPbBr_3$ quantum dots (QDs) were dispersed in an acrylate-based resin matrix and the QD active film was laminated between two transparent resin layers. Utilizing the pulse height spectra method, a light yield of up to 21 500 photons per MeV at room temperature was observed for the $CsPbBr_3$ QD-resin composites. The discrepancy in light yield between these studies may result from variations in nanocrystal concentration, matrix composition, and fabrication techniques, but also represent the challenge of accurately measuring light yield in perovskite–polymer composites.

Doping in perovskites helps to tune their optical and electronic properties, allowing for optimization of their applications as scintillators. Wu *et al.* investigated the use of Ce^{3+} ion doping in $CsPbBr_3$ NCs to enhance light yield and stability for high-resolution X-ray imaging applications.[83] The $CsPbBr_3$ NCs were synthesized using the hot injection method and the $CsPbBr_3$-polyvinylidene fluoride (PVDF) scintillator films were fabricated by dispersing the perovskite NCs into a PVDF film using suction filtration. It was found that Ce^{3+} ion doping has a positive influence on the light yield for up to 8% doping concentration, followed by a weakening at higher doping levels. This effect was attributed to the modification of defect states induced by Ce^{3+} doping, which influences the bandgap of the host lattice. The study reported that the light yield of the doped $CsPbBr_3$ NCs was about 33 000 photons per MeV, which was about 2 times more than that of the bare $CsPbBr_3$ NCs. The light yield was measured using the comparison method with Ce:LuAG scintillator as the reference material. A spatial resolution of 580 lp mm^{-1} was demonstrated for the scintillator films. An application of the scintillator films for high resolution X-ray imaging in biology and microelectronics was also demonstrated (Fig. 5e, f and g).

5.2 2D lead-based metal halide composites

Two-dimensional hybrid halide perovskites show great potential for a variety of optoelectronic applications, including solar cells,[141] light-emitting diodes (LEDs),[142] and photodetectors.[143] Compared to traditional 3D perovskites, two-dimensional halide perovskites offer advantages in scintillator applications due to their potential for enhanced stability achieved through organic spacer cations positioned between the perovskite layers. However, their performance is often hindered by poor charge transport, as the same insulating nature of these organic spacer cations that provides stability can also impede charge movement.[44,144,145] Nevertheless, 2D perovskite–polymer composites for scintillator applications have been reported.[146–148]

A study on the improved stability of 2D perovskites in water was reported by Zheng *et al.*[105] The 2D perovskites were synthesized using the acid precipitation method. In their study, they prepared stable water-repellent 2D metal halide perovskite scintillators by modifying them with long-chain hydrophobic organic cations and doping engineering. Mn doping was used to improve the scintillation performance and radiation stability of the 2D metal halide perovskites. While Mn-$(C_4H_9NH_2)_2PbBr_4$ and Mn-$(C_8H_{17}NH_2)_2PbBr_4$ lost their luminous properties when dispersed in water, the perovskites with long-chain hydrophobic organic cations, Mn-$(C_{12}H_{25}NH_2)_2PbBr_4$ and Mn-$(C_{18}H_{37}NH_2)_2PbBr_4$ exhibited bright luminescence even when immersed in water.

This difference was attributed to the superior water resistance of hydrophobic long-chain organic ammonium ions. It was shown that this waterproof characteristic allows for the development of hydrophobic perovskite scintillators suitable for underwater X-ray imaging applications. The synthesized Mn-$(C_{12}H_{25}NH_3)_2PbBr_4$ (Mn-DA_2PbBr_4) perovskites showed a PLQY of up to 76.29%. Further, a flexible scintillator film was fabricated by dispersing the Mn-DA_2PbBr_4 perovskites in the PMMA polymer precursor solution. The scintillator was used for underwater X-ray imaging and showed a spatial resolution up to 10 lp mm^{-1}. The light yield was measured to be 35 292 photons per MeV using the comparison method, with the BGO crystal scintillator as the reference material.

Shao *et al.* investigated the enhancement in the scintillation performance of 2D butylammonium lead bromide perovskite, (BA_2PbBr_4) with manganese (Mn) doping.[106] The 2D Mn^{2+} doped BA_2PbBr_4 perovskites were synthesized using the acid precipitation method. An optimal Mn^{2+}doping content of 10% was determined for enhanced energy transfer efficiency and scintillation performance, leading to a maximum PLQY of 57.58%. The introduction of Mn^{2+} impurity ions into the lattice, replaces Pb^{2+}, forming an octahedral coordination environment and enables additional emitters characterized by

the spin-forbidden $^4T_{1g}$ to $^6A_{1g}$ transition, thereby enhancing luminescence efficiency. It was also demonstrated that Mn^{2+} doping results in a large Stokes shift and therefore leads to a reduction in the self-absorption phenomenon observed in the 2D BA_2PbBr_4 perovskite. To fabricate the composite scintillation screens, the Mn^{2+} activated 2D perovskites were dispersed in the PMMA polymer precursor solution. The composites exhibited a high spatial resolution of 10 lp mm^{-1}, with an emission peak at 610 nm, which matched the sensitivity range of silicon-based sensor arrays, making it one of the highest long-wavelength emissions among perovskites and its derivative scintillator materials. The light yield was measured to be ~85 000 photons per MeV using the comparison method with BGO crystal and LYSO:Ce scintillator as the reference material.

5.3 Lead-free metal halide composites

Lead halide perovskite materials, like $CsPbBr_3$, have shown promise for enhancing X-ray sensitivity but are hindered by limitations, such as stability issues, self-absorption, and toxicity concerns. Among these, the toxicity concerns due to the presence of lead poses risks to both health and the environment, impeding commercialization efforts. Developing low-toxic or lead-free alternatives is crucial for advancing X-ray detection technologies. Efforts to substitute the Pb metal cation with elements like Sn, Cu, Mn, and Sb have been reported[52,149,150] (Table 2). Cao *et al.* reported the use of lead free tin based perovskites for scintillator applications.[89] Two-dimensional tin halide perovskites $(C_8H_{17}NH_3)_2SnBr_4$, were synthesized using an acid based solvochemical method with nearly 100% quantum yield and a decay time of 3.34 μs. The cytotoxicity of $(C_8H_{17}NH_3)_2SnBr_4$ was found to be lower than $CsPbBr_3$ perovskites, minimizing environmental and human health risks. The perovskite polymer composites were prepared by dispersing the $(C_8H_{17}NH_3)_2SnBr_4$ in the PMMA polymer precursor solution. These composites enabled image acquisition with a resolution of 200 μm and a sensitivity of 104.23 μGys^{-1} using standard CCD cameras, highlighting the promising potential of $(C_8H_{17}NH_3)_2SnBr_4$ perovskites for cost-effective, non-toxic, and high-resolution X-ray imaging applications.

A class of perovskites being explored as alternatives to traditional lead-based scintillators are lead free double perovskites.[87] In double perovskite structures with $A_2MM'X_6$ composition, A represents univalent element like Cs, M denotes univalent metallic elements like Na, Au, Ag and Cu, M′ signifies trivalent metallic elements such as Bi, Sb, Tb and rare-earth, and X represents a halide. Wang *et al.* explored the application potential of the Cerium doped $Cs_2NaTbCl_6$ perovskites in X-ray imaging and detection.[88] The $Cs_2NaTbCl_6$ double perovskite single crystals were synthesized using the hydrothermal method. To prepare the composite films, $Ce:Cs_2NaTbCl_6$ single crystals were ground into powder and then mixed with the acrylic pressure-sensitive adhesive. The scintillator films demonstrated a detection limit of 30 $nGys^{-1}$ and a spatial resolution of 10 lp mm^{-1}. The light yield of the $Ce:Cs_2NaTbCl_6$ crystals was measured to be 52 153 photons per MeV using the

Table 2 Scintillation properties of lead-free metal halide perovskites and their polymer composites

Material	Synthesis method of emitter	Synthesis method of composite/film : polymer	Emission (nm)	Light yield (photons per MeV); method used	Detection limit ($nGys^{-1}$)	Spatial resolution (lp mm^{-1} or μm)	Decay time (μs)	Radiation Hardness (residual RL %; dose (Gy))	Ref.
$((C_8H_{17}NH_3)_2SnBr_4)$	Acid based solvochemical	Dispersion : PMMA	596		104 230	200 μm	3.34		89
Cs_2ZrCl_6	Acid precipitation	Dispersion : PDMS	447	49 400; comparison	65	18	15.56	~94%; 18.14	107
Cs_2AgI_3:Cu	Antisolvent	Dispersion : PDMS	470	82 900; comparison	77.8	16.2	0.192	90%; 0.235	104
$Cs_3Cu_2I_5$	Antisolvent	Dispersion : PDMS	445	48 800; comparison	48.6	17 (MTF = 0.2)	~0.97		100
$Cs_3Cu_2I_5$	Antisolvent	Dispersion : PDMS	445	46 000; comparison	96.54	8.6	0.947	>99%; 12.42	101
$Cs_3Cu_2I_5$	Antisolvent	Dispersion : polystyrene	452		63	7.3		>95%; 1.27	102
$Cs_3Cu_2I_5$	Ball milling	Dispersion : PDMS	445	123 736; comparison		6.8 (MTF = 0.2)	0.96	>99%; 0.66	120
Rb_2CuBr_3	Modified LARP	Dispersion : polystyrene	385				61.04		111
$Cs_3Cu_2I_5$:Tl	*In situ*	*In situ* : PMMA	445	48 800; comparison	305	16.3	7.663	>80%; 604.8	132
$Cs_3Cu_2Cl_5$:2%K^+	Hot injection	Dispersion : polystyrene	547		63.5 (SNR = 3)	5	107.57		84
(TBA)$CuCl_2$ and (TBA)$CuBr_2$	*In situ*	*In situ* : PVDF	507	23 373; comparison			28.7		115
			497	24 134; comparison			232.05		
$TEA_2Cu_2Br_4$	Precipitation	Dispersion : PMMA	462	7623; comparison (for polycrystal)			58		112
$((C_{38}H_{34}P_2)MnBr_4)$ single crystal	Solvent diffusion	Dispersion : PDMS	517	66 256; comparison	461.1	322 μm	318	>99%; 1.28	113
$(BTPP)_2MnBr_4$ single crystal	Slow solvent evaporation	Dispersion : PDMS	515	53 000; comparison (for SC)	89.9	10.1 (MTF = 0.2)	300		114
$(C_{24}H_{20}P)_2MnBr_4$	*In situ*	*In situ* : TPU	520		608	14.5	316	>95%; 0.36	130
$(TEA)_2MnCl_4$ single crystal	Antisolvent	Dispersion : PDMS	524	12 000; comparison (for SC)	664 (SNR = 3)	3.5	2030		103
$(TBA)_2MnCl_4$ single crystal			512	21 000; comparison (for SC)	381 (SNR = 3)	5.6	3830		
$Cs_2Na_{0.9}Ag_{0.1}LuCl_6:Dy^{3+}$ single crystal	Hydrothermal	Dispersion : acrylic	~579	8332; comparison (for SC)	123.79	11.2 (MTF = 0.2)	3160		91
$Cs_2CdBr_2Cl_2$:5%Mn^{2+} single crystal	Hydrothermal	Dispersion : PDMS	593	64 950; comparison (for SC)	17.82	12.3 (MTF = 0.2)	70.74	>99%; 0.116	92
$Cs_2NaTbCl_6$:Ce single crystal	Hydrothermal	Dispersion : acrylic	548	52 153; comparison (for SC)	30	10	5690	~93%; 152.24	88

comparison method with the LYSO crystal scintillator as the reference material (Table 2). The doped perovskites demonstrated about 25% higher light yield than the undoped perovskites.

A lead-free double perovskite, Cs_2ZrCl_6, was explored for its scintillator applications by Zhang *et al.*[107] In this work, Cs_2ZrCl_6 nanograins were synthesized using the acid precipitation method. The Cs_2ZrCl_6 exhibited high thermally activated delayed fluorescence (TADF) emission with a PLQY of 70%, with an emission at 447 nm and Stokes shift of 190 nm. The Cs_2ZrCl_6 nanograins were dispersed in the PDMS polymer precursor mixture to create flexible films with adjustable thickness *via* spin coating. The Cs_2ZrCl_6@PDMS flexible films demonstrated a light yield of 49 400 photons per MeV, spatial resolution of 18 lp mm^{-1} and a low detection limit of 65 $nGys^{-1}$ (Table 2). The light yield was measured using the comparison method, using LYSO:Ce as the reference material (Fig. 6a). The X-ray irradiation stability of the scintillation

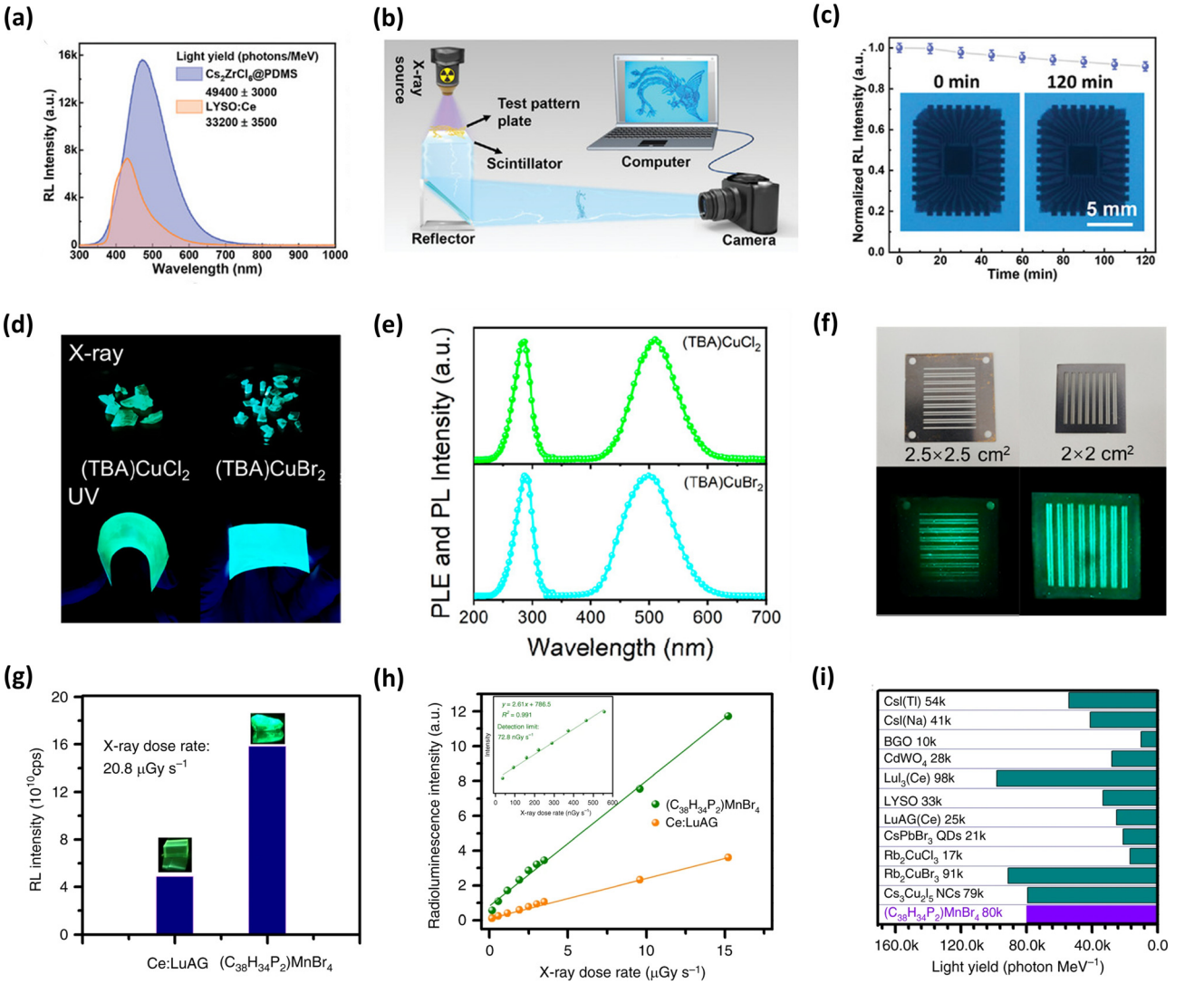

Fig. 6 Characteristics of lead-free metal halide polymer composites for scintillator applications. (a) Radioluminescence spectra of the Cs_2ZrCl_6-PDMS composite scintillator films and LYSO:Ce. Here, the light yield of the scintillator film is obtained using the comparison method. (b) A schematic of the X-ray imaging system used for the scintillator film. (c) X-ray irradiation stability of the scintillator films. Inset shows the X-ray images of a chip obtained using the scintillator films before and after X-ray irradiation. Reproduced with permission from ref. 107. Copyright 2021 Royal Society of Chemistry. (d) Lead-free organic zero-dimensional copper halide (TBA)CuX_2 (where TBA represents tetrabutylammonium cation and X represents Cl or Br) crystals (top) and scintillator films (bottom) under UV illumination. (e) Photoluminescence excitation and emission spectra of the (TBA)CuX_2 (X = Cl or Br) single crystals. (f) X-ray images of metallic masks obtained using the (TBA)CuX_2/PVDF composite scintillator films. Reproduced with permission from ref. 115. Copyright 2021 American Chemistry Society. (g) Comparison of the radioluminescence (RL) intensities of the reference Ce:LuAG and $(C_{38}H_{34}P_2)MnBr_4$ under the same X-ray dose rate. (h) Dose rate dependence of the RL intensity of standard reference Ce:LuAG and $(C_{38}H_{34}P_2)MnBr_4$. The inset shows the detection limit measurement of $(C_{38}H_{34}P_2)$ $MnBr_4$ under low X-ray dose. (i) Scintillator light yield comparison of $(C_{38}H_{34}P_2)MnBr_4$ and previously reported and commercially available scintillators. Reproduced with permission from ref. 113. Copyright 2020 Springer Nature.

films was tested by measuring the radioluminescence (RL) intensity after 120 minutes of continuous irradiation (Fig. 6b and c). The RL intensity showed a drop of only 6%, and X-ray imaging using the films didn't show any significant change before and after the irradiation.

Another emerging material for lead free X-ray scintillators are copper based metal halides, which exhibit reduced reabsorption effects and non-toxicity.[151,152] A copper-based metal halide which has been explored for scintillator applications is $Cs_3Cu_2I_5$. The $Cs_3Cu_2I_5$'s low-dimensional electronic structure facilitates the formation of self-trapped excitons (STEs) due to the lattice's Jahn–Teller distortion.[153] Self-trapped excitons (STEs) are localized excitations within a material where the electron and hole, created by the absorption of light or other excitations, become tightly bound to each other due to interactions with the surrounding lattice. The formation of STEs leads to a large Stokes shift, reducing reabsorption effects and making the material more suitable for scintillator applications.

Zhou *et al.* reported on the potential of $Cs_3Cu_2I_5$ as a substitute for lead perovskites for application in X-ray scintillators.[100] High-purity $Cs_3Cu_2I_5$ powders were synthesized using the antisolvent method. To create scintillator films, the $Cs_3Cu_2I_5$ powders were ground into finer particles and mixed with PDMS precursors, then blade coated. Ethyl acetate was added to prevent $Cs_3Cu_2I_5$ particle aggregation and improve film morphology. The resulting large area films with 400 cm^2 area were tested for X-ray detection, showing a low detection limit of 48.6 $nGys^{-1}$. The zero-dimensional (0D) $Cs_3Cu_2I_5$ phase with blue emission, exhibits high sensitivity to moisture and transitions into the 1D $CsCu_2I_3$ phase, emitting yellow light, upon exposure to moisture. To assess the engineered flexible film's suitability for real-world applications, its resistance to water and high temperatures was examined. While the blue emission of $Cs_3Cu_2I_5$ powders diminished and shifted to yellow under high humidity conditions (approximately 95%), the $Cs_3Cu_2I_5$ scintillator film retained the strong blue emission. Moreover, the PL intensity of the $Cs_3Cu_2I_5$ scintillator film remained nearly unchanged during prolonged exposure to heat. $Cs_3Cu_2I_5$-PDMS flexible films for scintillator applications were also reported by Duan *et al.*[101] The $Cs_3Cu_2I_5$ microcrystals were synthesized using the antisolvent method. To fabricate the $Cs_3Cu_2I_5$-PDMS flexible films, the microcrystals were ground into nanoscale particles and mixed with PDMS precursors. The light yield of the $Cs_3Cu_2I_5$-PDMS flexible films was measured to be 46 000 photons per MeV using the comparison method with the LYSO:Ce crystal scintillator as the reference material. $Cs_3Cu_2I_5$-polystyrene scintillator films were also reported with a low detection limit of 63 $nGy_{air}s^{-1}$ and a high spatial resolution of 7.3 lp mm^{-1}.[102] The $Cs_3Cu_2I_5$ nanoparticles were synthesized using a green antisolvent method using ethanol and dimethyl sulfoxide (DMSO).

Rb_2CuBr_3 was also reported as an environmental friendly lead free alternative.[111] The Rb_2CuBr_3 powders were synthesized using a modified LARP method. The scintillator films were synthesized by dispersing the Rb_2CuBr_3 powders in the polystyrene precursor solution. Doping in lead free copper-based metal halides, using alkali metals, to improve the photoluminescent properties has been investigated. Han *et al.* investigated the effect of K^+ doping in the copper based $Cs_3Cu_2I_5$ metal halides.[84] K^+:$Cs_3Cu_2Cl_5$ nanosheets (NSs) were synthesized *via* the hot injection method. Structural and luminescence studies revealed that the introduction of K+ ions (2%) enhanced the atomic interactions within the $Cs_3Cu_2Cl_5$ NSs, resulting in improved photoluminescence quantum yield (PLQY) from 70.23% to 81.39% and enhanced relative luminescence (RL) intensity. Additionally, a flexible K^+:$Cs_3Cu_2Cl_5$ polystyrene composite film was fabricated by mixing the ground crystals with the polystyrene precursors. The films demonstrated a high spatial resolution of 5 lp mm^{-1}. A light yield of 48 800 photons per MeV was also reported for 0.1% Tl doped $Cs_3Cu_2I_5$-PMMA scintillator films prepared using the *in situ* method.[132] The light yield was measured using the comparison method with the CsI:Tl scintillator as the reference material.

In addition to inorganic lead-free copper halides, organic zero-dimensional copper halides (TBA)CuX_2 (TBA = tetrabutylammonium cation and X = Cl, Br) were also investigated for scintillator applications by Lian *et al.*[115] The (TBA)$CuCl_2$ and (TBA)$CuBr_2$ single crystals (SCs) were synthesized through a slow solvent evaporation method conducted at room temperature. The composite film was fabricated using the *in situ* method by the solution blending of (TBA)CuX_2 (X = Cl, Br) precursor solution and PVDF polymer precursor solution (Fig. 6d and e). The light yield was found to be 24 134 photons per MeV for (TBA)$CuBr_2$ and 23 373 photons per MeV for (TBA)$CuCl_2$, using the comparison method, with Ce:LYSO scintillator as the reference. X-ray images of metallic masks obtained using the (TBA)CuX_2 PVDF composite films were also obtained (Fig. 6f).

Copper halides with tetraethylammonium (TEA) as the organic cation was also explored. Bin *et al.* in their study, synthesized crystalline $TEA_2Cu_2Br_4$ (TEA = tetraethylammonium) scintillator material using a liquid-phase cooling precipitation method.[112] The copper halide crystals were ground to powder form and mixed with the PMMA precursor solution to make the composite scintillator films. The light yield (LY) of $TEA_2Cu_2Br_4$ was measured to be 7623 photons per MeV using the comparison method, with CsI:Tl as the reference.

Another class of lead-free halides being investigated is composed of silver compounds. Silver possesses a higher atomic mass than copper, making it a promising alternative for lead-free applications. For instance, He *et al.* reported on the potential of Cu doped lead-free silver halide, Cs_2AgI_3 as an X-ray scintillator.[104] Both the Cs_2AgI_3 and the copper doped crystals were synthesized using a modified antisolvent method. The copper-doped perovskites exhibited a PLQY of 71%, while the undoped powders were nearly non-emissive. To make the scintillator screen, the Cu doped Cs_2AgI_3 polycrystalline powder was ground into powder form and mixed with the PDMS precursors and then spin coated on a glass substrate. The copper-doped scintillator film's light yield was measured to be 82 900

photons per MeV, using the comparison method with the commercial LYSO:Ce scintillator as the reference. The promising light yield of this silver-based halide was attributed to the higher atomic mass of the Cs, Ag, and I atoms, as well as the large Stokes shift of 166 nm. Furthermore, the carrier decay time of the copper-doped powders was found to be 192.8 ns, which is shorter than the microsecond lifetimes reported for other lead-free alternatives based on Copper and Rubidium. The scintillators also exhibited a low detection limit of 77.8 $nGys^{-1}$, which is lower than the dose rate required for standard medical X-ray diagnosis. Copper halides with tetraethylammonium (TEA) as the organic cation was also explored. Bin *et al.* in their study, synthesized crystalline $TEA_2Cu_2Br_4$ (TEA = tetraethylammonium) scintillator material using a liquid-phase cooling precipitation method.[112] The copper halide crystals were ground to powder form and mixed with the PMMA precursor solution to make the composite scintillator films. The light yield (LY) of $TEA_2Cu_2Br_4$ was measured to be 7623 photons per MeV using the comparison method, with CsI:Tl as the reference.

There is also interest in lead-free manganese-based metal halides for scintillator applications. Xu *et al.* reported the use of the organic manganese halide hybrid, ethylenebis-triphenylphosphonium manganese(II) bromide ($(C_{38}H_{34}P_2)MnBr_4$) for scintillator applications.[113] The manganese-based metal halide was synthesized using a room temperature solvent diffusion method, resulting in single crystals with a green emission peak at 517 nm and a high PLQY of 95%. Flexible scintillators were created by first grinding the $(C_{38}H_{34}P_2)MnBr_4$ single crystals into powder form and then mixing it with the PDMS precursors. A light yield of 66 256 photons per MeV and a detection limit of 461.1 $nGys^{-1}$ was reported for the films (Fig. 6g, h and i). The light yield of the scintillators was estimated using the comparison method by comparing the RL spectra of the organic manganese halide with a known reference material, Ce:LuAG. Lower dimensional manganese metal halides have also been explored for scintillator applications.[114] The researchers synthesized zero-dimensional (0D) $(BTPP)_2MnBr_4$ (BTPP = benzyltriphenylphosphonium) halides using a slow solvent evaporation method, aiming to exploit steric hindrance effects of the (BTPP) cation to enhance the luminescence efficiency. The synthesized 0D $(BTPP)_2MnBr_4$ hybrid single crystals showed an emission at 515 nm with a PLQY of 53%. The scintillation light yield of $(BTPP)_2MnBr_4$ single crystals was calculated to be 53 000 ± 2700 photons per MeV, with a known reference material, BGO, using the comparison method. To test the X-ray imaging capabilities, flexible scintillation screens were fabricated by mixing the ground $(BTPP)_2MnBr_4$ single crystal powders with the PDMS precursors. Also, the minimum detection limits for $(BTPP)_2MnBr_4$ was determined to be 89.9 $nGy_{air}s^{-1}$ (Table 2).

Lower-dimensional lead-free manganese-based metal halides with even higher PLQYs have been reported for scintillator applications. Cao *et al.* synthesized zero-dimensional manganese(II) based metal halides $(TEA)_2MnCl_4$ (TBA = tetraethylammonium) and $(TBA)_2MnCl_4$ (TBA = tetrabutylammonium) single crystals with green emission peaks at 524 nm and 512 nm, respectively, with PLQYs of approximately 65.07% and 99.96% using a room-temperature antisolvent method.[103] A light yield of 21 000 photons per MeV was measured for the $(TBA)_2MnCl_4$ single crystals using the comparison method, with Ce:GAGG as the reference. Flexible scintillators were also fabricated by mixing the ground crystals of $(TBA)_2MnCl_4$ with PDMS precursors. In addition to the dispersion method, Mn based scintillator films fabricated using the *in situ* method have also been reported.[130] The $(C_{24}H_{20}P)_2MnBr_4$-thermoplastic polyurethane (TPU) films showed a high PLQY of over 85%, with a detection limit of 0.608 $\mu Gy_{air}s^{-1}$ and a spatial resolution of 14.5 lp mm^{-1}.

Doping in lead-free metal halides for scintillator applications has been investigated. The effects of doping with Dy^{3+} and Ag^{+} on the lead free double perovskite crystals $Cs_2NaLuCl_6$ was investigated by Zhang *et al.*[91] The perovskite single crystals of $Cs_2NaLuCl_6$ were synthesized through a hydrothermal method. The incorporation of the typical afterglow activator Dy^{3+} resulted in a short yellow afterglow upon exposure to X-rays. Furthermore, $Cs_2NaLuCl_6$:Dy^{3+} was doped with different amounts of Ag^{+} to modify its afterglow duration, yielding $Cs_2Na_{0.9}Ag_{0.1}LuCl_6$:$Dy^{3+}$ with an afterglow lasting over 2 hours. Subsequently, the single crystals were ground to a powder, blended with an acrylic pressure-sensitive adhesive and later applied onto polyethylene terephthalate film substrates using the blade-coating method. The films achieved a spatial resolution of 11.2 lp mm^{-1}.

In addition to doping with Dy^{3+} and Ag^{+}, strategies to increase the scintillation performance of perovskites *via* Mn doping was reported. Mn^{2+} ion dopants offer a cost-effective enhancement of scintillator performance due to their efficient energy transfer and long carrier recombination time, which introduces additional radiative recombination channels within the scintillator lattice. Xu *et al.* investigated the effect of doping the 2D perovskite $Cs_2CdBr_2Cl_2$ with Mn^{2+} ions.[92] The 2D perovskite $Cs_2CdBr_2Cl_2$ single crystals were synthesized using the hydrothermal method. To assess $Cs_2CdBr_2Cl_2$:5% Mn^{2+}'s potential for X-ray imaging, the researchers fabricated flexible scintillator screens by mixing the ground $Cs_2CdBr_2Cl_2$ single crystals with the PDMS precursors. The scintillator films demonstrated a low detection limit of 17.82 $nGy_{air}s^{-1}$.

6. Perspective and conclusion

As the field of metal halide perovskite scintillators continues to evolve, several unresolved issues persist, requiring careful considerations. Here, we will outline some of these challenges and opportunities ranging from scalable, green synthesis of the emitter materials or their polymer composites to optimization of scintillation performance metrics and stability under varying environmental conditions. Addressing these challenges is essential for advancing our understanding of perovskite-based polymer composite scintillators and guiding future research directions, ultimately shaping the trajectory of advancements in this critical area of study.

6.1 Synthesis methods for the emitter materials

Scalable synthesis methods are essential for perovskite–polymer scintillator applications in vehicle scanning portals, medical screening, and other critical fields. The ability to produce large quantities of high-quality materials ensures consistent availability and cost-effectiveness, facilitating widespread adoption and integration into various industries for enhanced safety and security measures. Among the synthesis methods discussed, the most reported is the LARP method, likely due to its cost-effectiveness and ability to operate at low temperatures, meeting the practical requirements of perovskite NC synthesis.

While the LARP method is a scalable approach, it still necessitates the use of toxic solvents, which can be environmentally harmful. An alternative scalable method that minimizes the use of toxic solvents, that has been reported, is the mechanochemical method of ball milling. Previous studies have investigated ball milling for lead-based perovskites[119] and lead free metal halides[154] and also studied the impact of ligand addition on their photoluminescent properties.[155] However, further research is needed to fully explore the potential of this method for scintillator applications. In addition to the choice of the synthesis method, the utilization of green solvents and the recycling of the byproducts materials is also crucial for scalability. While environmentally friendly synthesis methods for perovskite NCs have been explored,[156,157] it is also necessary to evaluate their performance for practical implementation in scintillator devices. In the context of lead-based perovskite scintillators, inspiration can be drawn from research on perovskite solar cells and their efforts towards sustainable synthesis techniques. This interdisciplinary approach provides valuable guidance for developing eco-friendly and effective nanocrystal synthesis methods for scintillator devices. Notably, research in solar cells has explored the use of solvents such as water, gamma-valerolactone(GVL), ethanol, isopropanol(IPA), and other environmentally friendly alternatives.[158,159] Additionally, in solar cell research there are ongoing efforts in recycling lead and developing methods for easy separation and reuse of waste byproducts, which can further contribute to the environmentally sustainable synthesis of perovskite materials for scintillator applications.[160]

In recent years, lead-free metal halides, such as copper and manganese-based compositions, have garnered attention for their potential application in scintillator technologies. This increasing focus on lead-free perovskite and metal halides for scintillator applications, alongside the adoption of green synthesis methods, signals a positive trend in the field. This combination not only addresses environmental concerns but also holds the potential to scale up production for scintillators, offering promising prospects for widespread deployment and significant advancements in radiation detection technologies.

6.2 Synthesis methods for the composites

As we saw in the discussion, for scintillator applications, the most reported method for perovskite polymer composite fabrication involves the dispersion of the nanocrystals in the polymer precursor solution. This mixture is further cast as a film using techniques such as spin coating, blade coating, or drop casting. However, scalability and achieving homogeneity pose considerable challenges in these processes, with non-uniform distribution leading to efficiency losses due to scattering. Efforts are undergoing to advance the use of perovskite polymer composites in various fields including optoelectronics, photovoltaics, light-emitting diodes (LEDs), and more. Here, we discuss some recently reported methods like deep dyeing[161] and extrusion methods[162] which can offer an alternative solution to conventional methods.

Deep dyeing, is a method which enables the incorporation of perovskite NCs into the polymer matrix through an *in situ* process, facilitating a more homogeneous dispersion of the luminescent material. A novel deep-dyeing strategy for fabricating perovskite–polymer composites was reported by our group.[40,161,163] This approach converts commercial solvent-resistant polymer matrices, such as polyethylene terephthalate (PET), into deep-dyed perovskite polymer composites (DDPPCs). The synthesis method involves immersing PET matrices in a prepared metal halide perovskite (MHP) precursor solution, followed by a high temperature swelling process to enable the solvent and solute to penetrate the polymer matrix (Fig. 7a). Subsequent deswelling and drying processes yield luminescent DDPPCs characterized by remarkable colour tunability and environmental stability (Fig. 7b).

An important advantage of deep dyeing, as demonstrated in this work, is its capacity to directly employ the polymer in the *in situ* method, thereby reducing the likelihood of aggregation, while the incorporation of ligands further ensures the uniform dispersion of the luminescent material throughout the polymer matrix. This method can be employed to produce composites with polymers boasting high thermal stability, like polyethylene terephthalate (PET) and is applicable for various applications requiring high-temperature tolerance and outstanding barrier properties.

However, the trade-off between loading percentage and transparency can present a challenge, necessitating further research to optimize both aspects. Specifically, more investigation into transparency enhancement techniques alongside improved loading strategies is required to adopt the deep dyeing method effectively. Another *in situ* approach without using any solvents, *via* an extrusion method was reported for use as a diffuser in LED backlights.[164] This method replaced the solution synthesis process by melting extrusion and could achieve a PLQY of 90% for the $CsPbBr_3$ polymer composites with a FWHM of 22 nm. This one step extrusion method was reported to be cost effective, colour tunable and scalable (Fig. 7c).[162] Perovskite–polymer composites fabricated with initial goals for efficient displays or lighting may also be applicable as radiation-hard scintillators, either immediately or through further customization.

6.3 Light management in perovskite–polymer composites

In the context of perovskite–polymer composite scintillators, the interplay of Rayleigh and Mie scattering phenomena is

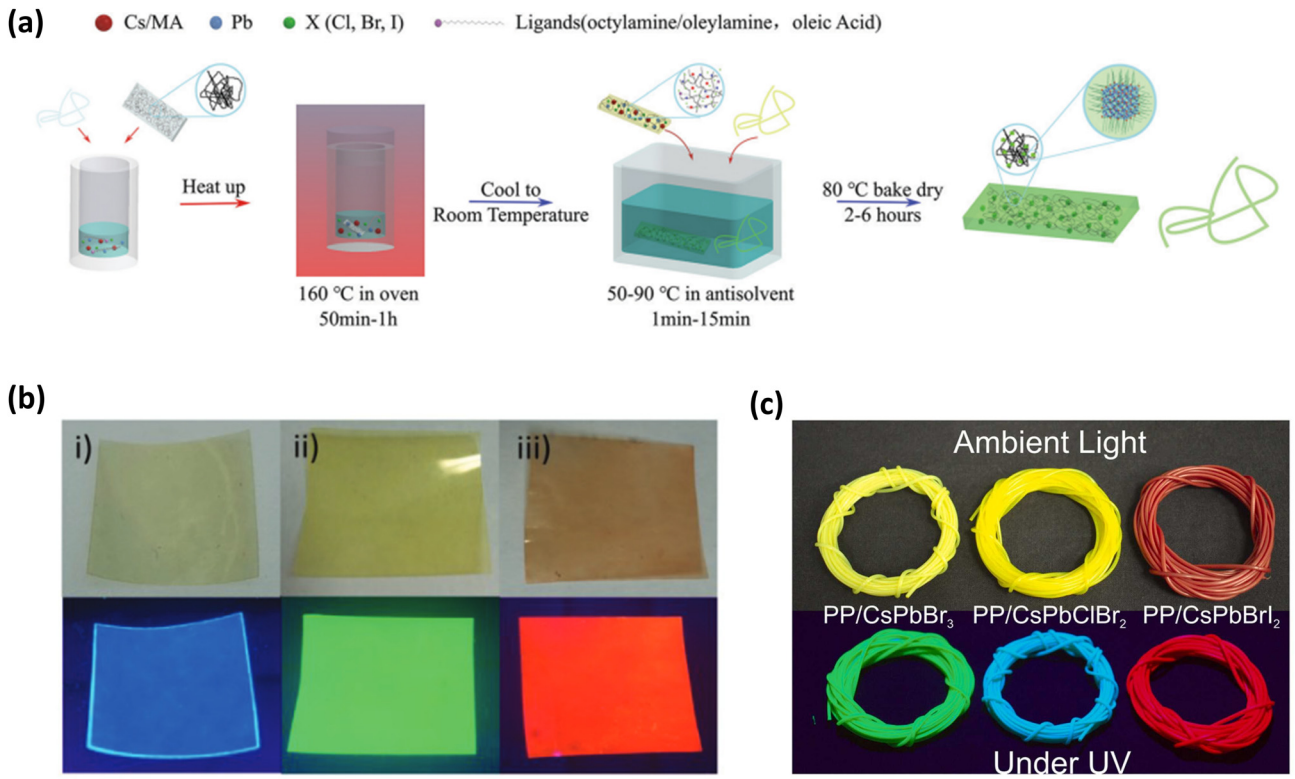

Fig. 7 Alternative synthesis methods of perovskite polymer composites for scintillator applications. (a) A schematic illustration of the deep dyeing synthesis method for perovskite polymer composites. Reproduced with permission from ref. 161. Copyright 2021 Royal Society of Chemistry. (b) Photographs of the colour tunable perovskite polymer composites obtained using the deep dyeing method under room light (above) and under UV illumination 365 nm (below). Reproduced with permission from ref. 167. Copyright 2020 John Wiley and Sons. (c) Photographs of the polypropylene perovskite composite filaments synthesized using the extrusion method under ambient light (top image) and UV light (bottom image). Reproduced with permission from ref. 162. Copyright 2022 Elsevier.

crucial for understanding light management.[165,166] Rayleigh scattering prevails when metal halide particles are significantly smaller than the scintillation wavelength, typically in the nanometre range. Conversely, as the particle size approaches the scintillation wavelength, Mie scattering becomes increasingly influential, leading to larger divergence angles and potential degradation in spatial resolution.

Therefore, careful control of particle size is paramount to minimize scattering effects and optimize the performance of composite scintillator materials. Uniform dispersion of metal halide NCs within the polymer matrix is crucial for achieving transparency and efficient light management. As we saw in the discussion, employing strategies such as *in situ* fabrication or surface ligand treatment of NCs can enhance dispersion uniformity and minimize agglomeration.[78,110,130,132] Additionally, controlling the refractive index difference between the metal halide NCs and the polymer matrix is vital for mitigating light scattering and improving transparency. Perovskite NCs typically have refractive indices ranging from 1.9 to 2.3,[168] depending on the specific composition and fabrication parameters. Therefore, exploration of high-refractive-index polymers,[169] holds promise for achieving optimal light management in perovskite–polymer composite scintillators. In addition, reabsorption effects can also significantly affect light outcoupling efficiency in composite scintillators, highlighting the importance of mitigating this phenomenon through material design and optimization. From our discussions so far, we have seen that lead-free metal halides, such as copper-based and manganese-based compounds, often exhibit a significant Stokes shift in comparison to metal halide perovskites. This is particularly advantageous in scintillator applications, as it minimizes self-absorption and enhances light outcoupling efficiency. Additionally incorporating dyes into the composite scintillator matrix can also be utilized to shift the emission spectrum, thereby minimizing self-absorption. Despite these efforts, continued investigation and innovation are necessary to improve the light outcoupling from perovskite–polymer composites for scintillator applications.

6.4 Stability tests for perovskite–polymer composites

Stability tests for perovskite–polymer composites encompass several critical factors, including irradiation stability, moisture and humidity resistance, heat stability, and fogging resistance. These aspects are essential for assessing the long-term per-

formance and reliability of the composites in real-world applications.

6.4.1. Radiation hardness. Perovskite–polymer composites experience degradation upon prolonged exposure to ionizing irradiation like Xray. As seen in the discussion, current efforts to improve the radiation hardness of perovskite–polymer composites show promise, with demonstrated reversibility after heat treatment. However, further efforts are needed to understand the chemical changes occurring in the perovskites within the composite after radiation exposure, particularly regarding aggregation and self-healing mechanisms under heat or UV treatment.[170]

6.4.2. Fogging resistance and thermal stability. In the field, some perovskite–polymer composites may degrade due to formation of internal fogging defects, leading to phase transitions, ion migration, reduced optical transmission, and decreased performance.[171,172] Fogging refers to the formation of microcracks or microvoids in a material due to prolonged exposure to hot and high humidity conditions, which allows water to permeate the material. When the material is then exposed to cooling cycles with repeated temperature drops, the trapped moisture can exacerbate the formation of cracks and voids, leading to visible fogging.[69] Accelerated aging coupled with optical and scintillation characterization should be used to evaluate the long-term performance and reliability of perovskite–polymer composites.[173,174]

As previously discussed, recent efforts have enhanced the moisture stability of these composites, with the composites showing minimal change in optical characteristics like photoluminescence (PL) and radioluminescence (RL) even after extended periods of water storage. However, further efforts are needed to bridge the gap between the most stable perovskite–polymer composites reported and the performance required to meet commercial application needs.

6.5 Light yield measurements

Measuring absolute light yield of scintillators present challenges due to variations in material properties, type and energy of incident radiation, calibration complexities and instrumentation constraints. Therefore, a meticulous experimental design and a detailed understanding scintillation physics are crucial for achieving accurate and reliable measurements.[175–177] Many research groups use radioluminescence to estimate the light yield by comparing the X-ray excited emission intensity of the studied material to that of reference materials with known light yields. While this approach can offer some insights into radioluminescence efficiency, comparing measurements across different studies is nearly impossible. Factors such as variation in irradiation geometry, light scattering, afterglow, non-proportionality, integration time and material's stopping power and density are often not considered when reporting and estimating light yields using this method. Thus, careful consideration is necessary when interpreting and comparing relative light yield measurements.

Employing absolute light yield measurements, such as the pulse height spectra method, can provide more reliable performance comparisons. However, standard Nuclear Instrumentation Modules (NIM) electronics are unable to collect all scintillation light from materials with slow decay times (>tens of μs), such as some copper- and manganese-based metal halides. In contrast, digital nuclear spectroscopy has proven successful in measuring the pulse height spectra of materials with milliseconds long decay times.[178] Therefore, using a combination of both measurement methods is suitable to accurately determine the light yield of new emerging scintillator materials.

6.6 Potential applications of MHP polymer composite scintillators

Metal halide perovskite polymer composite scintillators offer a promising alternative to traditional plastic scintillators in the near future. These composites maintain the flexibility and affordability of plastic scintillators while offering improved performance, including higher light yields and tunable emission wavelengths (Tables 1 and 2). These numbers are significantly greater than the 10 000 photons per MeV typically associated with plastic scintillators, like those based on polyvinyl toluene (PVT). Additionally, their tunable emission wavelengths are compatible with low-cost, high-efficiency photodetectors, such as silicon-based devices. These features make MHP-polymer composites well-suited for applications in portable radiation detectors, personal dosimeters, and security scanners, where plastic scintillators are currently utilized.

Looking ahead, with further improvements in their stability and detection efficiency, these perovskite–polymer composites could eventually replace well-established scintillators in demanding applications. Materials such as barium fluoride (BaF_2), sodium iodide with thallium doping (NaI(Tl)), cesium iodide (CsI) and gadolinium oxysulphide doped with praseodymium (GOS), which are commonly used in medical imaging and high-energy physics, could be supplanted by these advanced perovskite–polymer composites. As their performance continues to improve, these composites may offer a more efficient and cost-effective solution in applications where fast response, high density, light yield, and stability are critical.

Lastly, perovskite–polymer composites could enable new applications beyond replacing existing scintillators. Their flexibility and durability make them suitable for wearable radiation detectors in hazardous environments, offering real-time monitoring in a comfortable form. These materials could also be deployed in large-area, low-cost radiation detectors for environmental monitoring and safety, thanks to their scalability. Additionally, their emission tunability allows for advanced imaging systems optimized for specific radiation types, which could be useful in complex environments like space exploration or deep underground.

In conclusion, perovskite–polymer composites hold great promise for advancing indirect X-ray detection capabilities. The ongoing research and development efforts highlight the interest in harnessing these materials for improved X-ray

detection across medical imaging, security screening, and industrial applications. Overcoming remaining critical challenges, such as stability and scalability issues, will be pivotal for their widespread adoption in commercial settings.

Author contributions

Y. D. and S. J. S. conceived the review article and identified the themes together. S. J. S. conducted the literature review and wrote the initial draft. Y. T. and Y. T. contributed to theory sections. L. S. contributed to the theory and conclusion sections. Y. D. provided revision suggestions and refined the manuscript with S. J. S. Y. D. and S. T. W. acquired funding for the research.

Data availability

No primary research results, software or code have been included and no new data were generated or analysed as part of this review.

Conflicts of interest

There are no conflicts to declare.

Acknowledgements

Y. Dong is grateful for the support by UCF through seed grants (No. 63014223 and 20084201) for this work.

References

1 J. S. Manser, J. A. Christians and P. V. Kamat, *Chem. Rev.*, 2016, **116**, 12956–13008.
2 Y. Fu, H. Zhu, J. Chen, M. P. Hautzinger, X. Y. Zhu and S. Jin, *Nat. Rev. Mater.*, 2019, **4**, 169–188.
3 L. Zhang, L. Mei, K. Wang, Y. Lv, S. Zhang, Y. Lian, X. Liu, Z. Ma, G. Xiao, Q. Liu, S. Zhai, S. Zhang, G. Liu, L. Yuan, B. Guo, Z. Chen, K. Wei, A. Liu, S. Yue, G. Niu, X. Pan, J. Sun, Y. Hua, W.-Q. Wu, D. Di, B. Zhao, J. Tian, Z. Wang, Y. Yang, L. Chu, M. Yuan, H. Zeng, H.-L. Yip, K. Yan, W. Xu, L. Zhu, W. Zhang, G. Xing, F. Gao and L. Ding, *Nano-Micro Lett.*, 2023, **15**, 177.
4 Z. K. Tan, R. S. Moghaddam, M. L. Lai, P. Docampo, R. Higler, F. Deschler, M. Price, A. Sadhanala, L. M. Pazos, D. Credgington, F. Hanusch, T. Bein, H. J. Snaith and R. H. Friend, *Nat. Nanotechnol.*, 2014, **9**, 687–692.
5 N. Ahn, D. Y. Son, I. H. Jang, S. M. Kang, M. Choi and N. G. Park, *J. Am. Chem. Soc.*, 2015, **137**, 8696–8699.
6 M. A. Green, A. Ho-Baillie and H. J. Snaith, *Nat. Photonics*, 2014, **8**, 506–514.
7 A. Kojima, Y. Shirai and T. Miyasaka, *J. Am. Chem. Soc.*, 2009, **131**, 6050–6051.
8 P. Büchele, M. Richter, S. F. Tedde, G. J. Matt, G. N. Ankah, R. Fischer, M. Biele, W. Metzger, S. Lilliu, O. Bikondoa, J. E. Macdonald, C. J. Brabec, T. Kraus, U. Lemmer and O. Schmidt, *Nat. Photonics*, 2015, **9**, 843–848.
9 Y. Zhou, J. Chen, O. M. Bakr and O. F. Mohammed, *ACS Energy Lett.*, 2021, **6**, 739–768.
10 A. Datta, Z. Zhong and S. Motakef, *Sci. Rep.*, 2020, **10**, 20097.
11 D. Jenkins, *Radiation Detection for Nuclear Physics*, IOP Publishing, 2020.
12 A. Fogtman, S. Baatout, B. Baselet, T. Berger, C. E. Hellweg, P. Jiggens, C. La Tessa, L. Narici, P. Nieminen, L. Sabatier, G. Santin, U. Schneider, U. Straube, K. Tabury, W. Tinganelli, L. Walsh and M. Durante, *npj Microgravity*, 2023, **9**, 8.
13 E. Margui, I. Queralt and E. de Almeida, *Chemosphere*, 2022, **303**, 135006.
14 S. Akcay and T. Breckon, *Pattern Recognit.*, 2022, **122**, 108245.
15 M. D. Alam, S. S. Nasim and S. Hasan, *Prog. Nucl. Energy*, 2021, **140**, 103918.
16 M. Choquett, H. Rougeot, J.-P. Martin, L. Laperriere, Z. Shukri and B. T. Polischuk, *Proc. SPIE*, 2000, **3977**, 128–136.
17 U. N. Roy, G. S. Camarda, Y. Cui, R. Gul, G. Yang, J. Zazvorka, V. Dedic, J. Franc and R. B. James, *Sci. Rep.*, 2019, **9**, 7303.
18 M. Guerra, M. Manso, S. Longelin, S. Pessanha and M. L. Carvalho, *J. Instrum.*, 2012, **7**, C10004.
19 A. Brahme, *Comprehensive biomedical physics*, Newnes, 2014.
20 S. Program, *Personal Radiation Detectors (PRDs) and Spectroscopic PRDs Market and Survey Report*, National Urban Security Technology Laboratory (NUSTL), Department of Homeland Security, 2017.
21 P. M. Johns and J. C. Nino, *J. Appl. Phys.*, 2019, **126**, 040902.
22 M. F. Santarelli, A. Mori, M. Bertasi, V. Positano, A. Gimelli, M. Scipioni, P. Marzullo and L. Landini, *Electronics*, 2021, **10**, 2230.
23 L. Basiricò, A. Ciavatti and B. Fraboni, *Adv. Mater. Technol.*, 2021, **6**, 2000475.
24 A. Jana, S. Cho, S. A. Patil, A. Meena, Y. Jo, V. G. Sree, Y. Park, H. Kim, H. Im and R. A. Taylor, *Mater. Today*, 2022, **55**, 110–136.
25 C. V. Prasad, M. Labed, M. T. Alam Shamim Shaikh, J. Min, T. H. Vu Nguyen, W. Y. Song, K. J. Kim and Y. S. Rim, *Mater. Today Phys.*, 2023, **35**, 101095.
26 C. L. Melcher, R. A. Manente, C. A. Peterson and J. S. Schweitzer, *J. Cryst. Growth*, 1993, **128**, 1001–1005.
27 L. F. Blázquez, F. Aller, S. Vrublevskaya, J. Fombellida and E. Valtuille, *IFAC-PapersOnLine*, 2015, **48**, 852–857.

28 M. Nikl and A. Yoshikawa, *Adv. Opt. Mater.*, 2015, **3**, 463–481.
29 M. Hamel, *Plastic scintillators*, Springer, 2021.
30 M. Koshimizu, *Jpn. J. Appl. Phys.*, 2022, **62**, 010503.
31 M. Koshimizu, *Funct. Mater. Lett.*, 2020, **13**, 2030003.
32 M. Koshimizu, in *Plastic Scintillators: Chemistry and Applications*, Springer International Publishing, 2021, pp. 201–222.
33 Q. Chen, J. Wu, X. Ou, B. Huang, J. Almutlaq, A. A. Zhumekenov, X. Guan, S. Han, L. Liang, Z. Yi, J. Li, X. Xie, Y. Wang, Y. Li, D. Fan, D. B. L. Teh, A. H. All, O. F. Mohammed, O. M. Bakr, T. Wu, M. Bettinelli, H. Yang, W. Huang and X. Liu, *Nature*, 2018, **561**, 88–93.
34 O. D. I. Moseley, T. A. S. Doherty, R. Parmee, M. Anaya and S. D. Stranks, *J. Mater. Chem. C*, 2021, **9**, 11588–11604.
35 F. Zhou, Z. Li, W. Lan, Q. Wang, L. Ding and Z. Jin, *Small Methods*, 2020, **4**, 2000506.
36 Y. Li, W. Shao, X. Ouyang, Z. Zhu, H. Zhang, X. Ouyang, B. Liu and Q. Xu, *J. Phys. Chem. C*, 2019, **123**, 17449–17453.
37 S. Trivedi, D. Prochowicz, N. Parikh, A. Mahapatra, M. K. Pandey, A. Kalam, M. M. Tavakoli and P. Yadav, *ACS Omega*, 2021, **6**, 1030–1042.
38 A. Wibowo, M. A. K. Sheikh, L. J. Diguna, M. B. Ananda, M. A. Marsudi, A. Arramel, S. Zeng, L. J. Wong and M. D. Birowosuto, *Commun. Mater.*, 2023, **4**, 21.
39 L. Lu, M. Sun, T. Wu, Q. Lu, B. Chen and B. Huang, *Nanoscale Adv.*, 2022, **4**, 680–696.
40 Y. Wang, J. He, H. Chen, J. Chen, R. Zhu, P. Ma, A. Towers, Y. Lin, A. J. Gesquiere, S. T. Wu and Y. Dong, *Adv. Mater.*, 2016, **28**, 10710–10717.
41 F. Yao, P. Gui, Q. Zhang and Q. Lin, *Mol. Syst. Des. Eng.*, 2018, **3**, 702–716.
42 M. D. Birowosuto, D. Cortecchia, W. Drozdowski, K. Brylew, W. Lachmanski, A. Bruno and C. Soci, *Sci. Rep.*, 2016, **6**, 37254.
43 Y. Wei, Z. Cheng and J. Lin, *Chem. Soc. Rev.*, 2019, **48**, 310–350.
44 L. Mao, C. C. Stoumpos and M. G. Kanatzidis, *J. Am. Chem. Soc.*, 2019, **141**, 1171–1190.
45 S. Sun, M. Lu, X. Gao, Z. Shi, X. Bai, W. W. Yu and Y. Zhang, *Adv. Sci.*, 2021, **8**, 2102689.
46 S. Cheng, A. Beitlerova, R. Kucerkova, E. Mihokova, M. Nikl, Z. Zhou, G. Ren and Y. Wu, *ACS Appl. Mater. Interfaces*, 2021, **13**, 12198–12202.
47 R. Chiara, Y. O. Ciftci, V. I. E. Queloz, M. K. Nazeeruddin, G. Grancini and L. Malavasi, *J. Phys. Chem. Lett.*, 2020, **11**, 618–623.
48 L. A. Muscarella and E. M. Hutter, *ACS Energy Lett.*, 2022, **7**, 2128–2135.
49 D. J. Kubicki, D. Prochowicz, A. Pinon, G. Stevanato, A. Hofstetter, S. M. Zakeeruddin, M. Grätzel and L. Emsley, *J. Mater. Chem. A*, 2019, **7**, 2326–2333.
50 A. K. Guria, S. K. Dutta, S. D. Adhikari and N. Pradhan, *ACS Energy Lett.*, 2017, **2**, 1014–1021.
51 Q. Fan, G. V. Biesold-McGee, J. Ma, Q. Xu, S. Pan, J. Peng and Z. Lin, *Angew. Chem., Int. Ed.*, 2020, **59**, 1030–1046.
52 C. Zhou, M. Han, Y. Xiao, W. Tan, X. Jin, X. Wu, Y. Yang, S. Zhu, H. Lin, S. Lin, Q. Chen, Q. Liang, J. Hu, W. Zhang and Y. Jiang, *Mater. Sci. Eng., R*, 2023, **156**, 100756.
53 V. Morad, Y. Shynkarenko, S. Yakunin, A. Brumberg, R. D. Schaller and M. V. Kovalenko, *J. Am. Chem. Soc.*, 2019, **141**, 9764–9768.
54 Q. Zhou, W. Li, J. Xiao, A. Li and X. Han, *Adv. Funct. Mater.*, 2024, 2402902.
55 P. Lecoq, in *Particle Physics Reference Library: Volume 2: Detectors for Particles and Radiation*, 2020, pp. 45–89.
56 H. Hall, *Rev. Mod. Phys.*, 1936, **8**, 358–397.
57 L. Miaja-Avila, C. Lei, M. Aeschlimann, J. L. Gland, M. M. Murnane, H. C. Kapteyn and G. Saathoff, *Phys. Rev. Lett.*, 2006, **97**, 113604.
58 P. Eisenberger and P. M. Platzman, *Phys. Rev. A*, 1970, **2**, 415–423.
59 M. Cooper, P. Mijnarends, N. Shiotani, N. Sakai and A. Bansil, *X-ray Compton scattering*, OUP Oxford, 2004.
60 J. H. Hubbell, *Radiat. Phys. Chem.*, 2006, **75**, 614–623.
61 G. F. Knoll, *Radiation detection and measurement*, John Wiley & Sons, 2010.
62 M. J. Weber, *J. Lumin.*, 2002, **100**, 35–45.
63 R. Dossi, A. Ianni, G. Ranucci and O. J. Smirnov, *Nucl. Instrum. Methods Phys. Res., Sect. A*, 2000, **451**, 623–637.
64 V. B. Mykhaylyk, H. Kraus, V. Kapustianyk, H. J. Kim, P. Mercere, M. Rudko, P. Da Silva, O. Antonyak and M. Dendebera, *Sci. Rep.*, 2020, **10**, 8601.
65 T. Yanagida, *Proc. Jpn. Acad., Ser. B*, 2018, **94**, 75–97.
66 Q. He, C. Zhou, L. Xu, S. Lee, X. Lin, J. Neu, M. Worku, M. Chaaban and B. Ma, *ACS Mater. Lett.*, 2020, **2**, 633–638.
67 L. Pan, S. Shrestha, N. Taylor, W. Nie and L. R. Cao, *Nat. Commun.*, 2021, **12**, 5258.
68 P. B. Rose, A. Okowita, M. J. Lance and E. Sword, *IEEE Trans. Nucl. Sci.*, 2020, **67**, 1765–1771.
69 R. J. Cameron, B. G. Fritz, C. Hurlbut, R. T. Kouzes, A. Ramey and R. Smola, *IEEE Trans. Nucl. Sci.*, 2015, **62**, 368–371.
70 M. Loyd, M. Pianassola, C. Hurlbut, K. Shipp, N. Zaitseva, M. Koschan, C. L. Melcher and M. Zhuravleva, *Nucl. Instrum. Methods Phys. Res., Sect. A*, 2020, **949**, 162918.
71 Y. Zhang, R. Sun, X. Ou, K. Fu, Q. Chen, Y. Ding, L.-J. Xu, L. Liu, Y. Han, A. V. Malko, X. Liu, H. Yang, O. M. Bakr, H. Liu and O. F. Mohammed, *ACS Nano*, 2019, **13**, 2520–2525.
72 S. Cheng, A. Beitlerova, R. Kucerkova, M. Nikl, G. Ren and Y. Wu, *Phys. Status Solidi RRL*, 2020, **14**, 2000374.
73 S. Donati, in *Photodetectors*, John Wiley & Sons, Inc., 2020, pp. 103–174.
74 L. Protesescu, S. Yakunin, M. I. Bodnarchuk, F. Krieg, R. Caputo, C. H. Hendon, R. X. Yang, A. Walsh and M. V. Kovalenko, *Nano Lett.*, 2015, **15**, 3692–3696.
75 F. Zhang, H. Zhong, C. Chen, X.-G. Wu, X. Hu, H. Huang, J. Han, B. Zou and Y. Dong, *ACS Nano*, 2015, **9**, 4533–4542.

76 C. Murray, D. J. Norris and M. G. Bawendi, *J. Am. Chem. Soc.*, 1993, **115**, 8706–8715.
77 X. Li, F. Cao, D. Yu, J. Chen, Z. Sun, Y. Shen, Y. Zhu, L. Wang, Y. Wei, Y. Wu and H. Zeng, *Small*, 2017, **13**, 1603996.
78 K. Děcká, F. Pagano, I. Frank, N. Kratochwil, E. Mihóková, E. Auffray and V. Čuba, *J. Mater. Chem. C*, 2022, **10**, 12836–12843.
79 H. Chen, Q. Wang, G. Peng, S. Wang, Y. Lei, H. Wang, Z. Yang, J. Sun, N. Li, L. Zhao, W. Lan and Z. Jin, *Adv. Opt. Mater.*, 2022, **10**, 2102790.
80 B. Wang, J. Peng, X. Yang, W. Cai, H. Xiao, S. Zhao, Q. Lin and Z. Zang, *Laser Photonics Rev.*, 2022, **16**, 2100736.
81 J. X. Wang, X. Wang, J. Yin, L. Gutiérrez-Arzaluz, T. He, C. Chen, Y. Han, Y. Zhang, O. M. Bakr, M. Eddaoudi and O. F. Mohammed, *ACS Energy Lett.*, 2022, **7**, 10–16.
82 S. S. V. Naresh, H. Soh, J. Lee and N. Lee, *Mater. Today Nano*, 2023, 100364.
83 X. Wu, Z. Guo, S. Zhu, B. Zhang, S. Guo, X. Dong, L. Mei, R. Liu, C. Su and Z. Gu, *Adv. Sci.*, 2022, **9**, 2200831.
84 L. Han, B. Sun, C. Guo, G. Peng, H. Chen, Z. Yang, N. Li, Z. Ci and Z. Jin, *Adv. Opt. Mater.*, 2022, **10**, 2102453.
85 A. Rabenau, *Angew. Chem., Int. Ed. Engl.*, 1985, **24**, 1026–1040.
86 R. I. Walton, *Chem. – Eur. J.*, 2020, **26**, 9041–9069.
87 W. Zhu, W. Ma, Y. Su, Z. Chen, X. Chen, Y. Ma, L. Bai, W. Xiao, T. Liu, H. Zhu, X. Liu, H. Liu, X. Liu and Y. M. Yang, *Light: Sci. Appl.*, 2020, **9**, 112.
88 Z. Wang, X. Xu, S. Wang, H. Xu, W. Xu, Q. Zeng, G. Deng, Y. Jiang and S. Wu, *Chem. – Eur. J.*, 2021, **27**, 9071–9076.
89 J. Cao, Z. Guo, S. Zhu, Y. Fu, H. Zhang, Q. Wang and Z. Gu, *ACS Appl. Mater. Interfaces*, 2020, **12**, 19797–19804.
90 J. Ghosh, J. O'Neill, M. G. Masteghin, I. Braddock, C. Crean, R. Dorey, H. Salway, M. Anaya, J. Reiss, D. Wolfe and P. Sellin, *ACS Appl. Nano Mater.*, 2023, **6**, 14980–14990.
91 N. Zhang, R. Zhang, X. Xu, F. Wang, Z. Sun, S. Wang and S. Wu, *Adv. Opt. Mater.*, 2023, **11**, 2300187.
92 H. Xu, W. Liang, Z. Zhang, C. Cao, W. Yang, H. Zeng, Z. Lin, D. Zhao and G. Zou, *Adv. Mater.*, 2023, **35**, 2300136.
93 L. C. Schmidt, A. Pertegás, S. González-Carrero, O. Malinkiewicz, S. Agouram, G. Mínguez Espallargas, H. J. Bolink, R. E. Galian and J. Pérez-Prieto, *J. Am. Chem. Soc.*, 2014, **136**, 850–853.
94 S. Sun, D. Yuan, Y. Xu, A. Wang and Z. Deng, *ACS Nano*, 2016, **10**, 3648–3657.
95 J. Ye, Z. Li, D. J. Kubicki, Y. Zhang, L. Dai, C. Otero-Martinez, M. A. Reus, R. Arul, K. R. Dudipala, Z. Andaji-Garmaroudi, Y. T. Huang, Z. Li, Z. Chen, P. Muller-Buschbaum, H. L. Yip, S. D. Stranks, C. P. Grey, J. J. Baumberg, N. C. Greenham, L. Polavarapu, A. Rao and R. L. Z. Hoye, *J. Am. Chem. Soc.*, 2022, **144**, 12102–12115.
96 K. Hills-Kimball, H. Yang, T. Cai, J. Wang and O. Chen, *Adv. Sci.*, 2021, **8**, 2100214.
97 Y. Li, J. Shi, J. Zheng, J. Bing, J. Yuan, Y. Cho, S. Tang, M. Zhang, Y. Yao, C. F. J. Lau, D. S. Lee, C. Liao, M. A. Green, S. Huang, W. Ma and A. W. Y. Ho-Baillie, *Adv. Sci.*, 2020, **7**, 1903368.
98 J. Nie, C. Li, S. Zhou, J. Huang, X. Ouyang and Q. Xu, *ACS Appl. Mater. Interfaces*, 2021, **13**, 54348–54353.
99 F. Cao, D. Yu, W. Ma, X. Xu, B. Cai, Y. M. Yang, S. Liu, L. He, Y. Ke, S. Lan, K. L. Choy and H. Zeng, *ACS Nano*, 2020, **14**, 5183–5193.
100 Y. Zhou, X. Wang, T. He, H. Yang, C. Yang, B. Shao, L. Gutiérrez-Arzaluz, O. M. Bakr, Y. Zhang and O. F. Mohammed, *ACS Energy Lett.*, 2022, **7**, 844–846.
101 R. Duan, Z. Chen, D. Xiang, J. Si and X. Liu, *J. Lumin.*, 2023, **253**, 119482.
102 B. Wang, P. Li, Y. Zhou, Z. Deng, X. Ouyang and Q. Xu, *ACS Appl. Nano Mater.*, 2022, **5**, 9792–9798.
103 S. Cao, C. Li, P. He, J. A. Lai, K. An, M. Zhou, P. Feng, M. Zhou and X. Tang, *ACS Appl. Opt. Mater.*, 2023, **1**, 623–632.
104 T. He, Y. Zhou, X. Wang, J. Yin, L. Gutiérrez-Arzaluz, J. X. Wang, Y. Zhang, O. M. Bakr and O. F. Mohammed, *ACS Energy Lett.*, 2022, **7**, 2753–2760.
105 J.-X. Zheng, Z.-A. Zhou, T. Feng, H. Li, C.-H. Sun, N. Wang, Y. Tian, Y. Zhao and S.-Y. Zhou, *Rare Met.*, 2023, **43**, 175–185.
106 W. Shao, X. Wang, Z. Zhang, J. Huang, Z. Han, S. Pi, Q. Xu, X. Zhang, X. Xia and H. Liang, *Adv. Opt. Mater.*, 2022, **10**, 2102282.
107 F. Zhang, Y. Zhou, Z. Chen, M. Wang, Z. Ma, X. Chen, M. Jia, D. Wu, J. Xiao, X. Li, Y. Zhang, Z. Shi and C. Shan, *Adv. Mater.*, 2022, **34**, 2204801.
108 M. Gandini, I. Villa, M. Beretta, C. Gotti, M. Imran, F. Carulli, E. Fantuzzi, M. Sassi, M. Zaffalon, C. Brofferio, L. Manna, L. Beverina, A. Vedda, M. Fasoli, L. Gironi and S. Brovelli, *Nat. Nanotechnol.*, 2020, **15**, 462–468.
109 T. Skrypnyk, O. Viahin, I. Bespalova, O. Zelenskaya, V. Tarasov, V. Alekseev, S. Yefimova and O. Sorokin, *Radiat. Meas.*, 2023, **169**, 107028.
110 I. H. B. Braddock, M. A. S. Cheikh, J. Ghosh, R. E. Mulholland, J. G. O'neill, V. Stolojan, C. Crean, S. J. Sweeney and P. J. Sellin, *Nanomaterials*, 2022, **12**, 2141.
111 L. Han, H. Zhang, Y. Ning, H. Chen, C. Guo, J. Cui, G. Peng, Z. Ci and Z. Jin, *Chem. Eng. J.*, 2022, **430**, 132826.
112 X. Bin, L. Wu, J. Liu, T. Lin and R. Zeng, *Crystals*, 2022, **12**, 1799.
113 L. J. Xu, X. Lin, Q. He, M. Worku and B. Ma, *Nat. Commun.*, 2020, **11**, 4329.
114 W. Li, Y. Li, Y. Wang, Z. Zhou, C. Wang, Y. Sun, J. Sheng, J. Xiao, Q. Wang, S. Kurosawa, M. Buryi, D. John, K. Paurová, M. Nikl, X. OuYang and Y. Wu, *Laser Photonics Rev.*, 2023, **18**, 2300860.
115 L. Lian, X. Wang, P. Zhang, J. Zhu, X. Zhang, J. Gao, S. Wang, G. Liang, D. Zhang, L. Gao, H. Song, R. Chen, X. Lan, W. Liang, G. Niu, J. Tang and J. Zhang, *J. Phys. Chem. Lett.*, 2021, **12**, 6919–6926.

116 N. Salah, S. S. Habib, Z. H. Khan, A. Memic, A. Azam, E. Alarfaj, N. Zahed and S. Al-Hamedi, *Int. J. Nanomed.*, 2011, 863–869.
117 C. Suryanarayana, *Prog. Mater. Sci.*, 2001, **46**, 1–184.
118 L. Protesescu, S. Yakunin, O. Nazarenko, D. N. Dirin and M. V. Kovalenko, *ACS Appl. Nano Mater.*, 2018, **1**, 1300–1308.
119 K. V. Manukyan, A. V. Yeghishyan, D. O. Moskovskikh, J. Kapaldo, A. Mintairov and A. S. Mukasyan, *J. Mater. Sci.*, 2016, **51**, 9123–9130.
120 N. Li, Z. Xu, Y. Xiao, Y. Liu, Z. Yang and S. Liu, *Adv. Opt. Mater.*, 2022, **10**, 2102232.
121 Y. Xin, H. Zhao and J. Zhang, *ACS Appl. Mater. Interfaces*, 2018, **10**, 4971–4980.
122 S. Liang, M. Zhang, G. M. Biesold, W. Choi, Y. He, Z. Li, D. Shen and Z. Lin, *Adv. Mater.*, 2021, **33**, 2005888.
123 W. Ma, D. Liang, Q. Qian, Q. Mo, S. Zhao, W. Cai, J. Chen and Z. Zang, *eScience*, 2023, **3**, 100089.
124 T. C. Wang, S. Y. Yao, S. P. Yan, J. Yu, Z. Y. Deng, A. N. Yakovlev, B. Meng, J. B. Qiu and X. H. Xu, *ACS Appl. Mater. Interfaces*, 2023, **15**, 23421–23428.
125 G. I. Britvich, A. I. Peresypkin, V. I. Rykalin, V. G. Vasil'chenko, L. D. Kornylovskaya, S. A. Malinovskaya, V. T. Skripkina, V. M. Shershukov, E. G. Yushko, A. V. Kulichenko and A. I. Pyshchev, *Nucl. Instrum. Methods Phys. Res., Sect. A*, 1993, **326**, 483–488.
126 H. Guo, Y. Zhu, Q. Zhao, Q. Jiang, Y. Ma, J. Chen, L. Song, Z. Shi and C. Xu, *Sci. China Mater.*, 2023, **66**, 2004–2012.
127 D. Di, K. P. Musselman, G. Li, A. Sadhanala, Y. Ievskaya, Q. Song, Z.-K. Tan, M. L. Lai, J. L. MacManus-Driscoll and N. C. Greenham, *J. Phys. Chem. Lett.*, 2015, **6**, 446–450.
128 Q. Zhou, Z. Bai, W. G. Lu, Y. Wang, B. Zou and H. Zhong, *Adv. Mater.*, 2016, **28**, 9163–9168.
129 S. Chang, Z. Bai and H. Zhong, *Adv. Opt. Mater.*, 2018, **6**, 1800380.
130 K. Xia, P. Ran, W. Wang, J. Yu, G. Xu, K. Wang, X. Pi, Q. He, Y. Yang and J. Pan, *Adv. Opt. Mater.*, 2022, **10**, 2201028.
131 W. Chen, M. Zhou, Y. Liu, X. Yu, C. Pi, Z. Yang, H. Zhang, Z. Liu, T. Wang, J. Qiu, S. F. Yu, Y. Yang and X. Xu, *Adv. Funct. Mater.*, 2022, **32**, 2107424.
132 X. Hu, P. Yan, P. Ran, L. Lu, J. Leng, Y. M. Yang and X. Li, *J. Phys. Chem. Lett.*, 2022, **13**, 2862–2870.
133 P. H. H. Araújo, C. Sayer, R. Giudici and J. G. R. Poço, *Polym. Eng. Sci.*, 2002, **42**, 1442–1468.
134 F. Maddalena, A. Xie, X. Y. Chin, R. Begum, M. E. Witkowski, M. Makowski, B. Mahler, W. Drozdowski, S. V. Springham, R. S. Rawat, N. Mathews, C. Dujardin, M. D. Birowosuto and C. Dang, *J. Phys. Chem. C*, 2021, **125**, 14082–14088.
135 L. Wang, K. Fu, R. Sun, H. Lian, X. Hu and Y. Zhang, *Nano-Micro Lett.*, 2019, **11**, 52.
136 H. Jin, S. Yang, M. A. Iqbal and Y.-J. Zeng, *Nano Futures*, 2022, **6**, 042001.
137 K. Biswas, *Mater. Adv.*, 2022, **3**, 6791–6798.
138 K. Děcká, A. Suchá, J. Král, I. Jakubec, M. Nikl, V. Jarý, V. Babin, E. Mihóková and V. Čuba, *Nanomaterials*, 2021, **11**, 1935.
139 A. Magi, M. Koshimizu, A. Sato, Y. Fujimoto, S. Kishimoto, T. Yanagida and K. Asai, *Jpn. J. Appl. Phys.*, 2022, **61**, SB1036.
140 F. Maddalena, M. E. Witkowski, M. Makowski, A. Bachiri, B. Mahler, Y. C. Wong, C. Y. E. Chua, J. X. Lee, W. Drozdowski, S. V. Springham, C. Dujardin, M. D. Birowosuto and C. Dang, *ACS Appl. Mater. Interfaces*, 2021, **13**, 59450–59459.
141 X. Zhao, T. Liu and Y. L. Loo, *Adv. Mater.*, 2022, **34**, 2105849.
142 J. C. Blancon, J. Even, C. C. Stoumpos, M. G. Kanatzidis and A. D. Mohite, *Nat. Nanotechnol.*, 2020, **15**, 969–985.
143 J. Ghosh and P. K. Giri, *J. Phys.: Mater.*, 2021, **4**, 032008.
144 W. Fu, H. Chen and A. K. Y. Jen, *Mater. Today Nano*, 2021, **14**, 100117.
145 Y. Lekina and Z. X. Shen, *J. Sci.: Adv. Mater. Devices*, 2019, **4**, 189–200.
146 P. Wan, T. Jin, R. Gao, X. Ouyang, Z. Feng, G. Niu, J. Tang, L. Liu and X. Ouyang, *Adv. Funct. Mater.*, 2023, **34**, 2308263.
147 M. Xia, Z. Xie, H. Wang, T. Jin, L. Liu, J. Kang, Z. Sang, X. Yan, B. Wu, H. Hu, J. Tang and G. Niu, *Adv. Mater.*, 2023, **35**, 2211769.
148 J. Zheng, Y. Zeng, J. Wang, C. Sun, B. Tang, Y. Wu, Y. Zhang, Y. Yi, N. Wang, Y. Zhao and S. Zhou, *J. Am. Chem. Soc.*, 2021, **143**, 21302–21311.
149 X. Geng, Y. A. Chen, Y. Y. Li, J. Ren, G. H. Dun, K. Qin, Z. Lin, J. Peng, H. Tian, Y. Yang, D. Xie and T. L. Ren, *Adv. Sci.*, 2023, **10**, 2300256.
150 J. Zhou, K. An, P. He, J. Yang, C. Zhou, Y. Luo, W. Kang, W. Hu, P. Feng, M. Zhou and X. Tang, *Adv. Opt. Mater.*, 2021, **9**, 2002144.
151 W. Gao, G. Niu, L. Yin, B. Yang, J.-H. Yuan, D. Zhang, K.-H. Xue, X. Miao, Q. Hu, X. Du and J. Tang, *ACS Appl. Electron. Mater.*, 2020, **2**, 2242–2249.
152 X. Zhao, G. Niu, J. Zhu, B. Yang, J. H. Yuan, S. Li, W. Gao, Q. Hu, L. Yin, K. H. Xue, E. Lifshitz, X. Miao and J. Tang, *J. Phys. Chem. Lett.*, 2020, **11**, 1873–1880.
153 H. Chen, J. M. Pina, F. Yuan, A. Johnston, D. Ma, B. Chen, Z. Li, A. Dumont, X. Li, Y. Liu, S. Hoogland, Z. Zajacz, Z. Lu and E. H. Sargent, *J. Phys. Chem. Lett.*, 2020, **11**, 4326–4330.
154 L. Xie, B. Chen, F. Zhang, Z. Zhao, X. Wang, L. Shi, Y. Liu, L. Huang, R. Liu, B. Zou and Y. Wang, *Photonics Res.*, 2020, **8**, 768.
155 L. Protesescu, S. Yakunin, O. Nazarenko, D. N. Dirin and M. V. Kovalenko, *ACS Appl. Nano Mater.*, 2018, **1**, 1300–1308.
156 L. Zheng, K. Jiang, X. Li, P. Hong, K. Chen, H. Zhang, Y. Song and B. Luo, *J. Colloid Interface Sci.*, 2021, **598**, 166–171.
157 M. T. Hoang, *Green Chem.*, 2020, 3433–3440.

158 S. K. Podapangi, F. Jafarzadeh, S. Mattiello, T. B. Korukonda, A. Singh, L. Beverina and T. M. Brown, *RSC Adv.*, 2023, **13**, 18165–18206.
159 C. Worsley, D. Raptis, S. Meroni, A. Doolin, R. Garcia-Rodriguez, M. Davies and T. Watson, *Energy Technol.*, 2021, **9**, 2100312.
160 X. Wu, D. Zhang, X. Wang, X. Jiang, B. Liu, B. Li, Z. Li, D. Gao, C. Zhang, Y. Wang and Z. Zhu, *EcoMat*, 2023, **5**, e12352.
161 C. Zhang, Z. He, M. Mogensen, A. J. Gesquiere, C.-H. Chen, T.-L. Chiu, J.-H. Lee, S.-T. Wu and Y. Dong, *J. Mater. Chem. C*, 2021, **9**, 3396–3402.
162 A. N. Solodov, J. Shayimova, D. Balkaev, A. S. Nizamutdinov, K. Zimin, A. G. Kiiamov, R. R. Amirov and A. M. Dimiev, *Addit. Manuf.*, 2022, **59**, 103094.
163 J. He, Z. He, A. Towers, T. Zhan, H. Chen, L. Zhou, C. Zhang, R. Chen, T. Sun, A. J. Gesquiere, S. T. Wu and Y. Dong, *Nanoscale Adv.*, 2020, **2**, 2034–2043.
164 R. Fu and H. Zhong, *SID Symp. Dig. Tech. Pap.*, 2023, **54**, 414–416.
165 J. Jeong, B. Kim, M. J. Seol and S. Y. Kim, *Mater. Res. Bull.*, 2024, **175**, 112777.
166 X. Xu, Y. M. Xie, H. Shi, Y. Wang, X. Zhu, B. X. Li, S. Liu, B. Chen and Q. Zhao, *Adv. Mater.*, 2024, **36**, 2303738.
167 C. Zhang, Z. He, C. Gao, S.-T. Wu and Y. Dong, *SID Symp. Dig. Tech. Pap.*, 2020, **51**, 1303–1306.
168 J. K. Singh, S. K. Mandal and G. Banerjee, *J. Mater. Res.*, 2021, **36**, 1773–1793.
169 T. Higashihara and M. Ueda, *Macromolecules*, 2015, **48**, 1915–1929.
170 A. R. Kirmani, T. A. Byers, Z. Ni, K. VanSant, D. K. Saini, R. Scheidt, X. Zheng, T. B. Kum, I. R. Sellers, L. McMillon-Brown, J. Huang, B. Rout and J. M. Luther, *Nat. Commun.*, 2024, **15**, 696.
171 S. Cheng and H. Zhong, *J. Phys. Chem. Lett.*, 2022, **13**, 2281–2290.
172 Y. Gao, D. Lin, P. Liu, T. Shi and W. Xie, *Mater. Chem. Front.*, 2024, **8**, 785–799.
173 R. T. Kouzes, H. M. Cho, C. C. Cowles, G. Dib, P. E. Keller, J. E. Smart, P. J. Smith, B. J. Tucker, P. L. Feng, N. R. Myllenbeck and S. Payne, *Nucl. Instrum. Methods Phys. Res., Sect. A*, 2020, **954**, 161791.
174 C. C. Boyd, R. Cheacharoen, T. Leijtens and M. D. McGehee, *Chem. Rev.*, 2019, **119**, 3418–3451.
175 V. T. E. Sysoeva and O. Zelenskaya, *Nucl. Instrum. Methods Phys. Res., Sect. A*, 2002, **486**, 67–73.
176 N. Z. Galunov, *Funct. Mater.*, 2013, **20**, 304–309.
177 J. T. M. de Haas, P. Dorenbos and C. W. E. van Eijk, *Nucl. Instrum. Methods Phys. Res., Sect. A*, 2005, **537**, 97–100.
178 K. Watanabe, T. Yanagida, D. Nakauchi and N. Kawaguchi, *Jpn. J. Appl. Phys.*, 2021, **60**, 106002.